AIAA AVIATION Forum
August 2-6, 2021, VIRTUAL EVENT
AIAA AVIATION 2021 FORUM

10.2514/6.2021-2946

Separation Control by Co-Flow Wall Jet

Kewei Xu *, Yan Ren †, Gecheng Zha ‡
Dept. of Mechanical and Aerospace Engineering
University of Miami, Coral Gables, Florida 33124
E-mail: gzha@miami.edu

Abstract

This paper analyzes 2D differential and integral wall jet momentum equations for separation control. The analysis is used to investigate the separation control mechanism of co-flow wall jet, which utilizes an upstream tangential injection and downstream streamwise suction simultaneously to achieve zero-net-mass-flux flow control. The previous separation control guideline to obtain negative $\partial u^2/\partial y^2$ at the wall is found to be excessive for energy expenditure and may not be achievable, because $\partial u^2/\partial y^2 > 0$ is necessary in adverse pressure gradients at the wall regardless the flow is separated or attached. A more energy efficient separation control criterion is suggested to seek an attached elevated flow with $\tau_w > 0$ and $\partial u^2/\partial y^2 \geq 0$. The co-flow wall jet working mechanism includes three factors to offset adverse pressure gradients: 1) The spanwise vorticity established at the wall by the injection and suction is essential to enhance turbulent diffusion and the wall vorticity flux via the suction. 2) The streamwise mass flux provided by the wall jet enhances the streamwise inertia force. 3) The adverse pressure gradient enhances the streamwise inertia force and turbulent diffusion, which offset the adverse pressure gradient itself. Co-flow wall jet has a mechanism to grow its control capability with the increasing adverse pressure gradient. The NASA hump is numerically simulated and validated to support the theoretical analysis based on 2D Unsteady Reynolds averaged Navier-Stokes equations. The numerical analysis indicates that the turbulent diffusion plays the most dominant role to offset adverse pressure gradient.

* Ph.D. Candidate
† Post-doctoral Researcher
‡ Professor, AIAA associate Fellow

Nomenclature

AFC	Active Flow Control
APG	Adverse pressure gradient
BC	Boundary condition
C	The hump chord length
C_μ	Jet momentum coefficient, $\dot{m}_j\, U_j/(q_{ref}\, S)$
$CFWJ$	Co-flow wall jet
$FASIP$	Flow-Acoustics-Structure Interaction Package
FPG	Favorable pressure gradient
INJ	Injection
SUC	Suction
h	Slot height
LE	Leading Edge
LHS	Left Hand Side
Ma	Mach number
Re	Reynolds number
RHS	Right Hand Side
S	Inertia force
$URANS$	Unsteady-Reynolds-Averaged Navier-Stokes
V_j	Injection Jet velocity
U_{ref}	Reference velocity at inlet
U_∞	Freestream velocity away from wall
VP	Velocity Profile
$ZNMF$	Zero-Net Mass Flux

Greek

δ^*	Displacement thickness
γ	Air specific heats ratio
η	CFWJ pumping system efficiency
ρ_{ref}	Reference density
θ	Momentum thickness
τ_w	Wall shear stress

Subscript

c	Corrected to include the active flow control power
D	Differential momentum equation
I	Integral momentum equation
j	Injection Jet
t	Total value
ref	Reference parameters at hump inlet

∞	Freestream flow away from the wall
w	Wall

1 Introduction

Active Flow Control (AFC) has the potential to break through conventional fluid mechanics limitations and provides significant performance improvement to fluid systems [1]. AFC is to transfer external energy to the controlled flows in order to improve the performance of the flow systems. Since flow separation was first addressed by Prandtl [2], separation control has been an important application area of AFC. Understanding the separation control mechanism is of great importance for engineering practice to design a high efficiency flow system.

For turbulent boundary layer flow separation, achieving $\partial^2 u/\partial y^2 < 0$ based on the following wall boundary layer momentum equation has been used as the guideline for separation control as suggested by Gad-el-Hak and Bushnell [1, 3]:

$$\rho v_w \frac{\partial u}{\partial y}\bigg|_{y=0} - \left(\frac{\partial \mu}{\partial y}\frac{\partial u}{\partial y}\right)\bigg|_{y=0} + \frac{\partial p}{\partial x}\bigg|_{y=0} = \mu \frac{\partial^2 u}{\partial y^2}\bigg|_{y=0} \tag{1}$$

Fig. 1 (a) shows a concave velocity profile of an attached wall boundary layer with $\partial^2 u/\partial y^2 < 0$. Fig. 1 (b) shows a boundary layer at the onset of flow separation with $\partial^2 u/\partial y^2 > 0$ at the wall. Since the velocity far away from the wall must follow the main stream, the velocity profile must return to concave shape with an inflection point close to the wall. Eq. (1) indicates if the adverse pressure gradient (APG) is further increased beyond the separation onset value, the boundary layer will be separated with the velocity immediately above the wall having reversed direction, which will necessarily generate a positive $\partial^2 u/\partial y^2$ at the wall [1, 3]. Gad-el-Hak and Bushnell [1, 3] point out that $\partial^2 u/\partial y^2 < 0$ on the wall is a sufficient condition of an attached boundary layer. They stated their separation control guideline as "Namely, the objective is to keep $[\partial^2 u/\partial y^2]_{y=0}$ as negative as possible, or in other words to make the velocity profile as full as possible."[1] (p163).

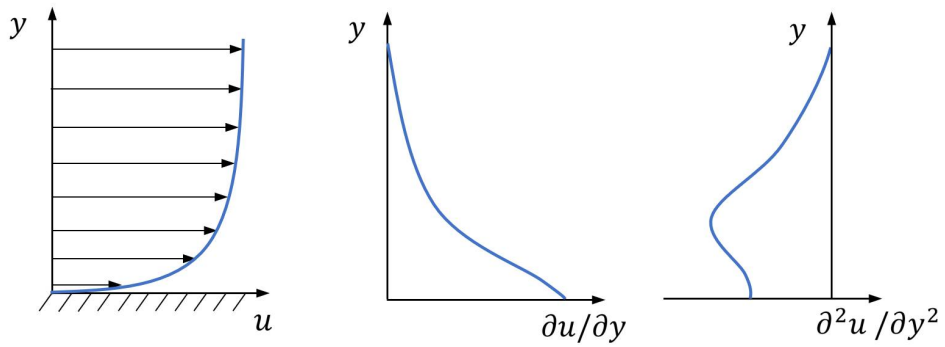

(a) Attached flow

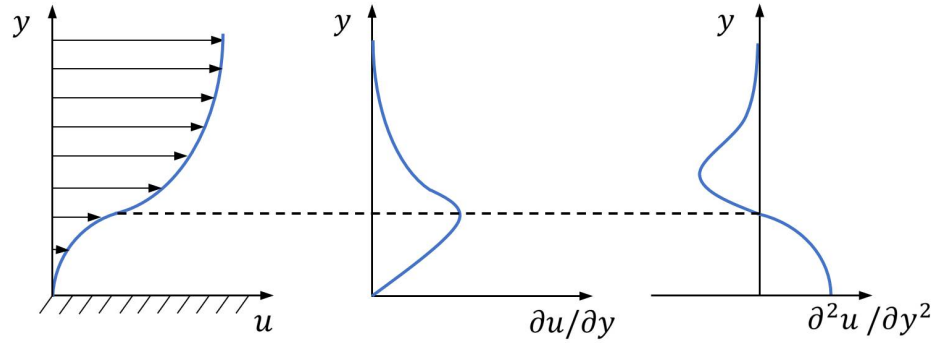

(b) Separation onset

Figure 1: Velocity profiles with different flow conditions

Schlichiting and Gersten [4] (p166) give the compatibility condition at the wall,

$$\left.\frac{\partial p}{\partial x}\right|_{y=0} = \mu \left.\frac{\partial^2 u}{\partial y^2}\right|_{y=0} \tag{2}$$

Eq. (2) can be directly obtained from Eq. (1) based on no slip wall condition and constant molecular viscosity within the viscous sublayer. This is a general equation for 2D flows regardless the flow is laminar or turbulent, separated or attached. It indicates that the sign of $\partial^2 u/\partial y^2$ at the wall is determined by the pressure gradient. The attached flow condition of $\partial^2 u/\partial y^2 < 0$ shown in Fig. 1 (a) means the flow has a favorable pressure gradient (FPG) and the velocity profile is "full" with no inflection point. For a flow in adverse pressure gradients (APG), $\partial^2 u/\partial y^2$ must be positive. Since flow separation can only occur in adverse pressure gradients [4], using $\partial^2 u/\partial y^2 < 0$ as separation control guideline is thus not related to the flow condition to be controlled. It requires that the flow is altered to have a local FPG, which may consume an excessive power. The main flow field pressure gradients are determined by the geometries and boundary conditions. Changing the pressure gradient locally may not even be achievable by active flow control because the main flow may have a high mass and momentum. Overall, there seems lack of a well defined criterion for separation control.

The purpose of this study is to investigate the Co-flow Wall Jet (CFWJ) AFC separation control mechanism. CFWJ is a recently developed zero-net-mass-flux AFC, which is shown to have high control effectiveness and low energy expenditure for airfoil lift enhancement, drag reduction, stall AoA increase, and separation removal [5, 6, 7, 8, 9, 10, 11, 12, 13, 14, 15, 16]. As sketched in Fig. 2 for an example of

CFWJ airfoil, CFWJ AFC draws a small amount of mass flow near the airfoil trailing edge, pressurizes and energizes it using a micro-compressor system embedded inside the airfoil, and then tangentially injects the same mass flow near the leading edge in the main flow direction.

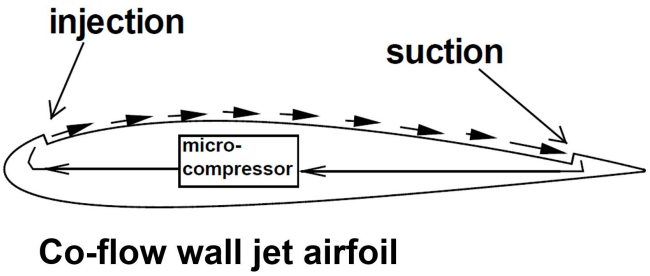

Figure 2: Schematics of the CFWJ airfoil

As shown in Fig. 2 , the co-flow wall jet has a tangential injection to the wall surface with a streamwise suction downstream. Hence the CFWJ is categorized as a wall jet. In this paper, the term "co-flow wall jet" means the same as the "co-flow jet (CFJ)", which is used in other previous publications [5, 6, 7, 8, 9, 10, 11, 12, 13, 14, 15, 16], CFWJ and CFJ are interchangeable. Since jet injection usually destabilizes the flow and makes the boundary layer turbulent, it is useful to give a brief overview of turbulent wall jets below.

1.1 Turbulent Wall Jets

Launder and Rodi [17] define a wall jet as a "boundary layer in which, by virtue of the initially supplied momentum, the velocity over some region in the shear layer exceeds that in the free stream". A wall jet can be viewed as having two shear layers: 1) the inner layer similar to conventional turbulent boundary layer; 2) the outer layer that is more like a free shear layer. As indicated by Launder and Rodi [17], the essential difference of a wall jet from conventional boundary layer is that the shear stress of the inner layer and outer layer has opposite sign and the maximum shear stress of the outer layer is usually several times larger than the wall shear stress. This also means that the inner and outer layer have opposite spanwise vorticity sign or counter rotating vortices. A turbulent wall jet always has a strong interaction between the two layers, which results in a shift of the zero shear stress position from the position of maximum velocity (where it would occur for a laminar wall jet) to a position beneath it [17, 18].

Wall jets are widely used for flow control such as the circulation control airfoil [19, 20, 21], co-flow jet active flow control [5, 6, 7, 8, 9, 10, 22], and aircraft upper surface blowing [23, 24, 25, 26]. There is a rich literature on wall jet studies pioneered by Forthmann with his first paper on wall jet in 1936 [27]. There are multiple wall jet studies after, including the important contributions of Glauert [28], Launder and Rodi [17], Bradshaw and Gee [29], McGahan [30], Newman [31], Patel and Newman [32], Irwin [18], Neuendorf and Wygnanski [33], Zhou et al [34], and Katz et al [35]. Most of these studies are focused on understanding of the fundamental physics behaviors of the wall jets either with or without external streams, such as the velocity scaling law, skin friction, eddy viscosity and shear stress distribution, shear layer growth rate, forced excitation, etc. Very few of the studies address the wall jet mechanism for separation control, even though it is well recognized that wall jet is effective to suppress flow separation due to energizing the boundary layer.

Among the various turbulent wall jet studies, the research of McGahan [30] is one of the few that investigates flow separation suppression from a wall jet perspective. McGahan experimentally tested several injection locations of the wall jet, including one at far upstream of the separation onset point, one at upstream and close to the onset point, and one at the separation onset point. McGahan claims that the most effective and efficient injection location is the one upstream and close to the separation onset point. McGahan also observes that a larger injection slot size reduces the required power for injection. He mentions that there should be an optimum slot size. Other than the general statement of energizing the boundary layer by tangential blowing, McGahan does not reveal the physical role how the wall jet suppress the flow separation. The criterion of the separation onset point used by McGahan [30] is the inception of the measured pressure plateau, which is usually a little downstream of the actual separation onset point with zero wall shear stress. His conclusions on the wall jet relative position about the separation onset point hence may not be accurate.

1.2 Co-Flow Wall Jet

As previously described, CFWJ AFC always comes in pair with an injection and suction to form a closed mass conservation system on the flow control plane. In other words, the CFWJ is a ZNMF flow control that combines the features of wall jets and boundary layer suction. Fig. 3 are the sketches showing the wall velocity profiles alternated by the CFWJ injection and suction effects: a) the boundary layer at separation onset with no CFWJ; b) the injection wall jet of CFWJ that shows a typical wall jet velocity profile with three counter rotating vortex layers. Establishing the near wall surface clockwise vorticity is necessary to attach a flow. The stronger the injection jet, the greater the vorticity; c) the streamwise suction of CFWJ. The CFWJ suction is located downstream to "pull" the flow in the streamwise direction. It also enhances the clockwise vorticity near the wall surface. The CFWJ suction is different from some widely used suction flow controls that withdraw the flow into the wall perpendicularly. It is thus termed streamwise suction.

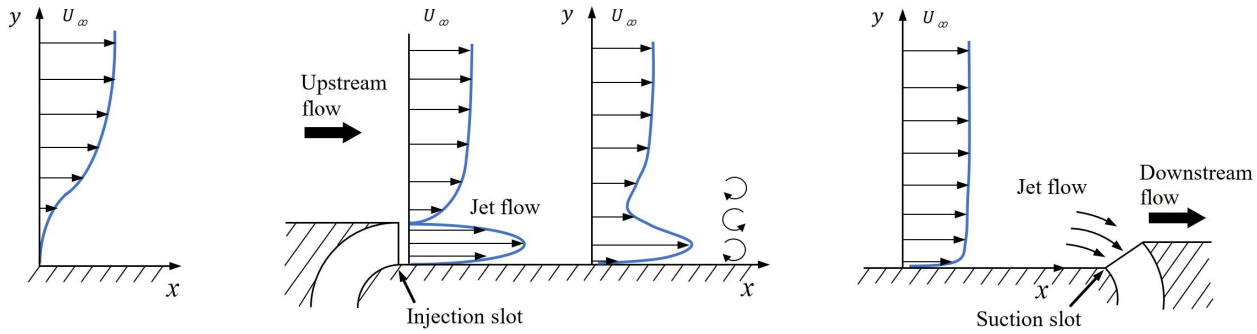

(a) Without CFWJ (b) CFWJ injection (c) CFWJ suction

Figure 3: Sketches for the CFWJ injection and suction effects

In the previous experimental and numerical studies [8, 9, 36, 37], it is observed that the CFJ airfoil can achieve a maximum lift coefficient exceeding the theoretical limit of potential flow, $C_{Lmax} = 2\pi(1 + t/c)$ [38]. The flow can remain attached up to angle of attack (AoA) of 70°-80°, at which the stagnation point of the airfoil is detached from the airfoil solid body due to ultra-high circulation. The APG is substantially higher than that of conventional airfoil stall limit, up to by an order of magnitude.

In other words, the high lift coefficient is achieved by suppressing the flow separation in extremely

severe APG. The questions to ask then include: 1) Why CFWJ can sustain such a high adverse pressure gradient? What is the mechanism? What are the factors contributing to this performance? Answering these questions is the motivation of this paper.

A literature survey is conducted to answer above questions as the first effort. Pioneered by Prandtl [2] for his boundary layer suction work, various studies as summarized in [1, 4] show that boundary layer suction generating negative transverse velocity v_w is effective to suppress flow separation. The rationale is that the term $\rho v_w \frac{\partial u}{\partial y}\Big|_{y=0}$ in Eq. (1) can offset the adverse pressure gradient if v_w is negative. Thus suction normal to the wall surface is widely studied to maximize v_w. Blowing normal to the wall is also used to reduce friction drag by creating "inviscid" flow [4] at the wall surface. To achieve this effect, the blowing needs to be in favorable pressure gradients and is thus usually implemented at the leading edge stagnation area [4]. Following the same strategy, Wiedemann and Gersten [39] implement both normal blowing and suction together in a cylinder with the normal blowing at the leading edge and normal suction at the trailing edge to reduce friction drag. The blowing flow rate is 9 times higher than the suction flow rate. It is expected that the blowing power required to overcome the high pressure in the stagnation region must be very high, but the energy consumption is usually not a focus since most of the past research pays more attention to the AFC effectiveness and less to the energy expenditure.

Overall, studies based on boundary layer momentum equation for separation control with tangential injection and suction like the co-flow wall jet is not well documented. This paper is to shed some light on this subject.

2 Separation Control Analysis

2.1 Separation Control Criterion

The previous discussion for Eq. (2) indicates that the sign of $\partial^2 u/\partial y^2$ on the wall is determined by the pressure gradient. Between the attached flow with favorable pressure gradient shown in Fig. 1 (a) and the onset condition with APG shown in Fig. 1 (b), all the flows are attached. It means that the flow remains attached in a range of APG until it reaches the critical value of the separation onset. That is why $\partial^2 u/\partial y^2 < 0$ is a sufficient condition for attached flow, not a necessary condition. However, $\partial^2 u/\partial y^2 > 0$ is a necessary condition of separated flows [1], but not a sufficient condition.

In other words, if a boundary layer has $\partial^2 u/\partial y^2 > 0$ at the wall, it could be well attached as long as the wall shear stress has $\tau_w > 0$, or $\partial u/\partial y > 0$, or $\omega_z < 0$. Fig. 4 illustrates an exaggerated example of such attached boundary layer velocity profile for clarity, which has $\partial^2 u/\partial y^2 > 0$ and $\partial u/\partial y > 0$. It has a rapid elevation of the velocity profile near the wall and an inflection point away from the wall indicated by the dash line. Away from the wall, the attached velocity profile quickly makes $\partial^2 u/\partial y^2$ negative to match the mean flow direction with a concave shape. A well attached boundary layer will have a large positive value of $\partial u/\partial y$ at the wall and the inflection point located very close to the wall. The middle photo of Fig. 5 shows such a velocity profile observed in the experiment of a diffuser conducted by Abernathy [40]. To facilitate the description, the attached flow with $\partial^2 u/\partial y^2 > 0$ is named "attached elevated flow" in this paper. According to Eq. (2), all attached flows in APG are attached elevated flows.

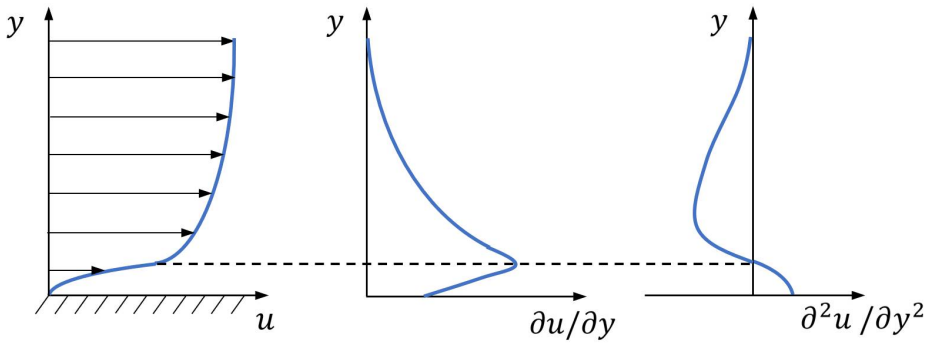

Figure 4: Attached flow with adverse pressure gradient

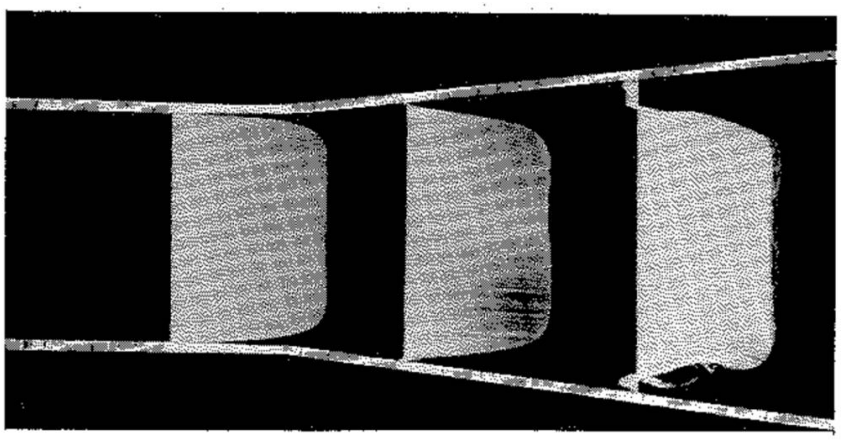

Figure 5: Experimental visualized velocity profile development from the attached flow (left and middle) to separated flow (right) in a diffuser [40]

A weak boundary layer will have a low value of $\partial u/\partial y$ and the inflection point moving away from the wall. When $\partial u/\partial y$ is reduced to zero, it is the separation onset point with $\tau_w = 0$ as shown in Fig. 1 (b). When $\partial u/\partial y$ is further decreased to be negative, the flow is separated with $\tau_w < 0$, or $\omega_z > 0$.

Due to the APG, $\partial^2 u/\partial y^2$ at the wall is positive and an inflection point necessarily exists in the velocity profile. Seeking $\partial^2 u/\partial y^2 < 0$ at the wall as the flow separation control criterion is unnecessary, excessive in energy consumption for the AFC, and may be unachievable. The sign of $\partial^2 u/\partial y^2$ does not uniquely determine attached flow status and is not an indicative criterion for separation control.

Based on the discussion above, a more energy efficient criterion for separation control may be summarized below. It is for both laminar and turbulent flows by manipulating the boundary layer velocity profiles.

1. The guideline is to seek attached elevated flows with adverse pressure gradients instead of attached flows with favorable pressure gradients.

2. The attached velocity profiles will have $\tau_w > 0$ ($\partial u/\partial y > 0$, $\omega_z < 0$) with $\partial^2 u/\partial y^2 \geq 0$. (The $\partial^2 u/\partial y^2 = 0$ includes zero pressure gradient cases.)

3. If $\partial u/\partial y < 0$, the flow is separated.

This separation control criterion does not require excessive energy to alter the sign of $\partial^2 u/\partial y^2$. The larger the velocity slope $\partial u/\partial y$ at the wall, the stronger the flow attached. Such a criterion seems obvious, but is necessary to be clearly for clarification.

To understand the flow control mechanism of CFWJ, it is necessary to analyze the wall jet momentum equations applicable to co-flow wall jets with the streamwise convection term considered in both partial and integral forms.

2.2 Turbulent Wall Jet Differential Momentum Equation

Assuming that the wall curvature is small, body force can be neglected, flow direction is from left to right ($u > 0$), x is the direction tangential to the wall surface, and y is the direction normal to the wall surface, the 2D incompressible turbulent wall jet momentum equation in x direction can be approximated as the following:

$$\rho u\frac{\partial u}{\partial x} + \rho v\frac{\partial u}{\partial y} + \frac{\partial p}{\partial x} = \frac{\partial \tau_{xy}}{\partial y} \tag{3}$$

Normalize Eq. (3) by using $\bar{u} = u/u_\infty$, $\bar{x} = x/L_\infty$, $\bar{y} = y/L_\infty$, $\bar{\mu} = \mu/\mu_\infty$, $\bar{p} = p/(\rho_\infty u_\infty^2)$ and $\bar{\rho} = \rho/\rho_\infty$. The wall jet momentum equation can be rewritten below with the non-dimensional variables. The over-line bars are omitted for clarity.

$$\rho u\frac{\partial u}{\partial x} + \rho v\frac{\partial u}{\partial y} + \frac{\partial p}{\partial x} = \frac{1}{Re}\frac{\partial \tau_{xy}}{\partial y} \tag{4}$$

or

$$\rho u\frac{\partial u}{\partial x} + \rho v\frac{\partial u}{\partial y} + \frac{\partial p}{\partial x} = \frac{1}{Re}\frac{\partial(\mu\frac{\partial u}{\partial y})}{\partial y} \tag{5}$$

Eq. (5) is originated from the Reynolds Averaged Navier-Stokes equations with the Bousinesque eddy viscosity assumption. The gradient of the normal stress τ_{xx} is neglected for being small as typically treated for wall boundary layer. The viscosity coefficient μ includes the molecular viscosity and turbulent eddy viscosity. Eq. (5) is similar to the one used by Glauert [28] for turbulent wall jet except Glauert only considered the zero pressure gradient without the $\partial p/\partial x$ term. Eq. (5) can be further expanded as:

$$\rho u\frac{\partial u}{\partial x} + \rho v\frac{\partial u}{\partial y} - \frac{1}{Re}\frac{\partial \mu}{\partial y}\frac{\partial u}{\partial y} + \frac{\partial p}{\partial x} = \frac{1}{Re}\mu\frac{\partial^2 u}{\partial y^2} \tag{6}$$

$$R + \frac{\partial p}{\partial x} = \frac{1}{Re}\mu\frac{\partial^2 u}{\partial y^2} \tag{7}$$

$$LHS_D = \frac{1}{Re}\mu\frac{\partial^2 u}{\partial y^2} \tag{8}$$

where R is the summation of the first three terms of Eq. (6), which is the resultant factor to offset the pressure gradient. LHS_D is the summation of all the terms on the left hand side (LHS) of Eq. (6).

This equation plays the same guidance role for wall jet flow control as Eq. (1) for boundary layer flow control. The difference between Eq. (6) and Eq. (1) is that Eq. (6) has the term $\rho u \cdot \partial u/\partial x$, which is neglected in Eq. (1) for boundary layer flow control. All the other terms also exist in the boundary layer momentum Eq. (1). However, the turbulent co-flow wall jet substantially enhances all the first three terms of Eq. (6) by imposing a high momentum injection jet or streamwise suction.

The turbulent wall jet momentum Eq. (6) is well known. However as mentioned in the last section, for tangential blowing and streamwise suction, the analysis of each term's contribution to offset the adverse pressure gradient for separation control is not well documented. This paper studies their effects first based on the physical analysis, and then seeks evidence support from the numerical analysis in next section.

The first two terms on the LHS of Eq. (6) are the convective terms, which are responsible to transport the wall jet momentum in streamwise and transverse direction. The second term $\rho v \cdot \partial u/\partial y$ is in the similar order of magnitude to the first term due to the high velocity gradient imposed by the CFWJ. The third term is a part of the momentum diffusion from the RHS of Eq. (5) due to the turbulent eddy viscosity gradient. This term is negligible for laminar flow since the viscosity is fairly constant, but is dominant for turbulent co-flow wall jet mixing due to the rapid growing rate of turbulent eddy viscosity near the wall.

For separation control, the first three terms on the LHS are responsible for offsetting the adverse pressure gradient and attaching the flow with a positive wall shear stress, which is the control objective. However, Eq. (6) is not a simple cause-effect relation. The diffusion terms on the RHS as well as on the LHS play a crucial role to transfer the momentum inward to energize the boundary layer and outward to induce the main flow.

Eq. (6) can be also expressed in terms of spanwise vorticity as:

$$\omega_z = \frac{\partial v}{\partial x} - \frac{\partial u}{\partial y} \approx -\frac{\partial u}{\partial y} \tag{9}$$

This is because a co-flow wall jet injection tangential to the wall surface has $\frac{\partial v}{\partial x} << \frac{\partial u}{\partial y}$ except in the region of the suction slot entrance. The wall jet momentum Eq. (6) upstream of the suction slot may be rewritten as:

$$\rho u\frac{\partial u}{\partial x} - \rho v\omega_z + \frac{\omega_z}{Re}\frac{\partial \mu}{\partial y} + \frac{\partial p}{\partial x} = \frac{\mu}{Re}\frac{\partial^2 u}{\partial y^2} \tag{10}$$

2.3 CFWJ Working Mechanism in a Nutshell

The CFWJ working mechanism to offset adverse pressure gradients may be explained based on Eq. (6) and (10) with the following three factors:

1. CFWJ establishes sufficient clockwise spanwise vorticity $\omega_z < 0$, or $\partial u/\partial y > 0$ at the wall by tangential injection and streamwise suction. $\omega_z < 0$ is essential to contribute to the third term, the turbulent diffusion. It also contributes to the second term, the wall vorticity flux, via the streamwise suction ($v < 0$).

2. The wall jet provides sufficient streamwise mass flux $\rho u > 0$, which contributes to the first term, the streamwise inertia force.

3. The adverse pressure gradient enhances the $\partial u/\partial x < 0$, which contributes to the first term, the streamwise inertia force. The adverse pressure gradient also enhances $\partial \mu/\partial y > 0$ [41], the eddy viscosity gradient near the wall. This is a crucial factor for the third term, the turbulent diffusion. In other words, adverse pressure gradients enhance the effectiveness and efficiency of CFWJ. When the APG is increased, the control capability of the CFWJ to offset the APG also increases with the APG, provided the factor 1) and 2) are established.

The following sections elaborate the mechanism with more explanations.

2.3.1 Injection Effect

For a forced tangential turbulent wall jet injection, once the jet is injected into the external stream, the streamwise velocity variation of the turbulent wall jet is subject to the streamwise pressure gradient. For an adverse pressure gradient, $\partial u/\partial x < 0$, the first term in Eq. (10) $\rho u \cdot \partial u/\partial x$ is negative to offset the adverse pressure gradient. $\rho u \cdot \partial u/\partial x$ represents the streamwise inertia force inserted by the wall jet to the boundary layer.

For the tangential injection, the normal velocity component v is small. Based on the incompressible flow continuity equation:

$$\frac{\partial v}{\partial y} = -\frac{\partial u}{\partial x} \tag{11}$$

That means $v > 0$ near the wall under an adverse pressure gradient. Thus the second convection term of Eq. (10) will increase the adverse pressure gradient. Even though $v << u$, the convention term $\rho v \cdot \partial u/\partial y$ can be at a similar order of magnitude to the $\rho u \cdot \partial u/\partial x$ term because the velocity gradient $\partial u/\partial y$, or the vorticity ω_z is large due to the wall jet.

However, a tangential injection is still the most effective way to minimize v. If the jet injection has an angle extruding to the main flow, there could be a large positive v. The convection term $\rho v \cdot \partial u/\partial y$ in Eq. (6), or the vorticity flux $-\rho v \omega_z$ in Eq. (10) will be positive and large. Such a non-tangential injection will increase the flow blockage to the main flow, decrease the clockwise spanwise vorticity near the wall, and enlarge the adverse pressure gradient instead of reducing it. For example, a strong jet injection 90° normal to the main flow may create a large flow blockage and separation.

Near the wall, the term $\partial \mu/\partial y$ is positive and large due to the rapid increase of turbulent eddy viscosity enhanced the adverse pressure gradient [41]. The turbulent diffusion term $\partial u/\partial y \cdot \partial \mu/\partial y/Re$ thus plays a dominant role of offsetting the adverse pressure gradient and mixing to transfer the high kinetic energy of the wall jet inward to increase the momentum of the boundary layer and outward to induce the main flow. At the maximum velocity position of the wall jet away from the wall, the velocity gradient or

the spanwise vorticity approaches zero. But the streamwise inertia force at that position will be more dominant to overcome the adverse pressure gradient due to the increased streamwise velocity. In addition to the turbulent diffusion term, the streamwise inertia force term $\rho u \cdot \partial u/\partial x$ also grows with the adverse pressure gradient as described in Section 2.3. The larger the adverse pressure gradient $\partial p/\partial x$, the larger the streamwise inertia force term to offset the adverse pressure gradient due to $\partial u/\partial x$ being more negative.

2.3.2 Suction Effect

For the CFWJ streamwise suction as sketched in Fig. 3 (c), the velocity entering into the suction slot is usually not completely tangential to the main flow streamwise direction, but has a significant velocity component normal to the wall surface. This is to minimize the drag created by streamwise suction reactionary force [15, 42]. Drag matters for external airfoil flow, but may not matter as much for internal flow, which cares more about energy loss. To avoid a large drag due to suction, one may intend to use a suction slot tangential to the wall surface, which will have a vertical suction. A vertical suction forces the flow to have a sharp turning at the suction location and may create a local flow blockage. Liu and Zha [42] did a trade study for the transonic CFJ-RAE2822 airfoil and found that a suction slot angle of 12° about the wall surface (0° is fully tangential to the wall surface) is the most efficient and effective. In other words, for CFWJ streamwise suction, both the velocity components normal and tangential to the streamwise direction are significant.

For the CFWJ suction as illustrated in Fig. 3 (c), it may not have a protruding velocity profile like the injection unless when it is very close to the injection slot. Since the vertical velocity component entering into the suction slot is negative, the convection term $\rho v \cdot \partial u/\partial y$ in Eq. (6) will be negative. The streamwise inertia force term $\rho u \cdot \partial u/\partial x$ and the diffusion term play the same roles as for the injection jet. That is, for the CFWJ suction, all the first three terms in Eq. (6) will contribute significantly to offset the adverse pressure gradient. This streamwise suction mechanism to offset the APG also grows with the APG.

Above analysis indicates that both CFJ injection and suction can be effective to overcome adverse pressure gradient and suppress flow separation. But the analysis is based on an essential condition that a full velocity profile with a positive velocity gradient $\frac{\partial u}{\partial y}$ ($\omega_z < 0$) can be established by either the injection or suction. This requires the injection or suction be placed near the flow separation onset where the flow has adverse pressure gradient, but is not massively separated yet and does not consume too much energy to establish the positive velocity gradient. Placing the injection or suction in the deep separation region will not be efficient or effective to establish the required velocity gradient. The flow separation onset point is usually also the maximum adverse pressure gradient location. This gives another reason to apply the AFC near the flow separation onset point to suppress the separation before it starts.

2.4 Turbulent Wall Jet Integral Momentum Equation

The wall jet Eq. (3) and (4) describe the balance between the adverse pressure gradient and the other terms in the differential momentum equation. The lump effect can be obtained by integrating the momentum equation across the wall jet. The integral form of the non-dimensional wall jet momentum equation derived by Coles [43] based on Eq. (4) is given below:

$$\rho \frac{d(u_\infty^2 \theta)}{dx} + \rho u_\infty \delta^* \frac{du_\infty}{dx} = \frac{\tau_w}{Re} \tag{12}$$

Where δ^* is the displacement thickness, θ is the momentum thickness. The derivation of Coles [43] for Eq. (12) is quoted in the Appendix with permission.

Eq. (12) can be expanded to

$$(2\theta + \delta^*)\rho u_\infty \frac{du_\infty}{dx} + \rho u_\infty^2 \frac{d\theta}{dx} = \frac{\tau_w}{Re} \tag{13}$$

To introduce pressure gradient to the integral equation, the freestream Euler equation below is substituted to Eq. (13),

$$\rho u_\infty \frac{du_\infty}{dx} = -\frac{dp}{dx} \tag{14}$$

We have

$$\rho u_\infty^2 \frac{d\theta}{dx} - (2\theta + \delta^*)\frac{dp}{dx} = (2\theta + \delta^*)(\mathcal{Q}\frac{d\theta}{dx} - \frac{dp}{dx}) = (2\theta + \delta^*)(\mathcal{S} - \frac{dp}{dx}) = \frac{\tau_w}{Re} \tag{15}$$

Where, $\mathcal{S} = \mathcal{Q}\frac{d\theta}{dx}$, and

$$\mathcal{Q} = \frac{\rho u_\infty^2}{2\theta + \delta^*} \tag{16}$$

$\mathcal{Q}$ represents the convection terms expressed by the dynamic pressure enhanced by the wall jet momentum and displacement thickness. A CFWJ will enhance the clockwise vorticity at the wall and reduce θ and δ^*, which augments the $\mathcal{Q}$ factor.

Eq. (15) can be further written as

$$LHS_I = \frac{\tau_w}{Re} \tag{17}$$

LHS_I is the summation of the left hand side of Eq. (15). If $LHS_I > 0$, $\tau_w > 0$, the flow is attached. If $LHS_I < 0$, $\tau_w < 0$, the flow is separated. This is the same separation control criterion as given in Section 2.1. Referring to Fig. 4 , a positive τ_w is a necessary condition to define an attached flow. Assuming both δ^* and θ are positive, if $\mathcal{S} > \frac{dp}{dx}$, then $\tau_w > 0$, the flow is attached. If $\mathcal{S} < \frac{dp}{dx}$, then $\tau_w < 0$, the flow is separated.

Eq. (15) is consistent with the CFWJ working mechanism summarized in Section 2.3. The spanwise vorticity ω_z and streamwise mass flow will reduce θ and δ^* to increase $\mathcal{Q}$ factor and $\mathcal{S}$ factor. For a wall jet in adverse pressure gradient, $d\theta/dx$ is always positive due to boundary layer momentum loss. Similar to the streamwise inertia force term and the turbulent diffusion in the partial differential wall jet Eq. (10), the larger the adverse pressure gradient, the greater the $d\theta/dx$ term, which will increase $\mathcal{S}$ to offset the APG. This is the APG offsetting mechanism of CFWJ from the integral momentum equation perspective.

2.4.1 Applying CFWJ near Separation Onset Point

At the separation onset point, the APG is usually the highest. It is critical to suppress the flow separation before it starts. The rationale to apply CFWJ near the separation onset location can be also explained based on the integral momentum equation: 1) The maximum APG will maximize $d\theta/dx$ to contribute to $\mathcal{S}$ factor. 2) The injection or suction will minimize the θ and δ^*. The main flow dynamic pressure is usually large at the beginning of the flow diffusion region before the velocity decreases further. All these effects will increase $\mathcal{Q}$ factor and $\mathcal{S}$ factor.

Even though it is desirable to apply either the CFWJ injection or suction near the separation onset point, it would be more efficient and effective to apply the CFWJ injection near the separation onset point and the suction downstream for three reasons: 1) The main-flow static pressure at the separation onset point may be near the lowest. It is efficient to make an injection to a low pressure location to establish the clockwise spanwise vorticity ω_z and mass flow ρu. 2) The downstream suction will be located at a location with higher pressure, which will make the suction more efficient. 3) The entire CFWJ may be immersed in the APG region, which is more favorable to enhance CFWJ as previously described.

3 Numerical Investigation of CFWJ NASA hump

This section numerically studies the NASA hump with CFWJ implemented to support above separation control analysis with qualitative and quantitative results.

3.1 Governing Equations

The governing equations for the CFD simulation are the unsteady Reynolds averaged Navier-Stokes equations (URANS) with one equation Spalart-Allmaras turbulence model [44], which are solved in a fully coupled manner using an implicit unfactored Gauss-Seidel line iteration to achieve high convergence rate. The normalized Navier-Stokes governing equations in generalized coordinates are given by:

$$\frac{\partial \mathbf{Q}}{\partial t}+\frac{\partial \mathbf{E}}{\partial \xi}+\frac{\mathbf{F}}{\partial \eta}+\frac{\mathbf{G}}{\partial \zeta}=\frac{1}{Re}\left[\frac{\partial \mathbf{R}}{\partial \xi}+\frac{\partial \mathbf{S}}{\partial \eta}+\frac{\partial \mathbf{T}}{\partial \zeta}\right]+S_\nu \tag{18}$$

where Re is the Reynolds number. The conservative variable vector $\mathbf{Q}$, invisid flux $\mathbf{E}$, viscous flux vector $\mathbf{R}$ are expressed as follows, and the rest can be expressed following the symmetric rule.

$$\mathbf{Q}=\frac{1}{J}\begin{bmatrix}\rho\\ \rho u\\ \rho v\\ \rho w\\ \rho e\\ \rho\hat{\nu}\end{bmatrix},\ \mathbf{E}=\frac{1}{J}\begin{bmatrix}\rho U\\ \rho u U+p\xi_x\\ \rho v U+p\xi_y\\ \rho w U+p\xi_z\\ (\rho e+p)U\\ \rho\hat{\nu}U\end{bmatrix},\ \mathbf{R}=\frac{1}{J}\begin{bmatrix}0\\ \tau_{xi}\xi_i\\ \tau_{yi}\xi_i\\ \tau_{zi}\xi_i\\ (u_j\tau_{ij}-q_i)\xi_i\\ \frac{\rho}{\sigma}(\nu+\hat{\nu})\frac{\partial\hat{\nu}}{\partial x_i}\xi_i\end{bmatrix}$$

The S_ν in Eq. (18) is the source term for the S-A model,

$$S_\nu = \frac{1}{J}\left[\frac{1}{Re}\left[-\rho\left(c_{w1}f_w - \frac{c_{b1}}{\kappa^2}f_{t2}\right)\left(\frac{\tilde{\nu}}{d}\right)^2\right]\right.$$
$$\left. + \frac{1}{Re}\left[\frac{\rho}{\sigma}c_{b2}\left(\nabla\tilde{\nu}\right)^2 - \frac{1}{\sigma}\left(\nu+\tilde{\nu}\right)\nabla\tilde{\nu}\bullet\nabla\rho\right] + Re\left[\rho f_{t1}\left(\Delta q\right)^2\right] + \rho c_{b1}\left(1-f_{t2}\right)\tilde{S}\tilde{\nu}\right] \tag{19}$$

Other auxiliary relations and coefficients for the S-A turbulence model can be found in [16, 44].

3.2 Navier-Stokes Equations Solver

The in-house high order CFD code Flow-Acoustics-Structure Interaction Package (FASIP) is used to solve the 2D Unsteady-Reynolds averaged Navier-Stokes equations. A 3rd order WENO scheme for the inviscid flux [45, 46, 47, 48, 49, 50] and a 4th order central differencing for the viscous terms [45, 49] are employed to discretize the Navier-Stokes equations. The low diffusion E-CUSP scheme suggested by Zha et al [46] based on the Zha-Bilgen flux vector splitting [51] is utilized with the WENO scheme to evaluate the inviscid fluxes. All the simulations in this study are conducted as unsteady time accurate simulations. The second order time accurate implicit time marching method with pseudo time and Gauss-Seidel line relaxation is used to achieve a fast convergence rate [50, 52]. Parallel computing is implemented to save wall clock simulation time [52, 53]. The FASIP code is intensively validated for CFWJ simulations [5, 7, 8, 10, 15, 53, 42, 54, 55, 56, 57, 58, 59]. The numerical results are presented with time average after the flows and all the aerodynamic forces become dynamically stable.

3.3 The NASA Hump

The NASA hump is widely used as a benchmark case to validate numerical algorithms and turbulence modeling [60] for flow control. The baseline hump configuration with no flow control is designed to have a converging section followed by a rapid area expansion downstream of the throat as shown in Fig. 6, which creates a severe diffusion and massive flow separation.

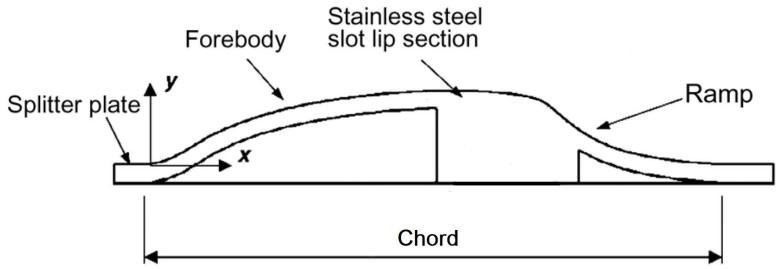

Figure 6: Geometry of hump upper surface [61]

3.4 Mesh and Boundary Conditions

The NASA hump geometry shown in Fig. 6 is a wall-mounted Glauert hump model and the computational domain is created based on the experiment set-up described in [61, 62]. The 2D computational domain is normalized by the hump chord (C) of 420mm (see Fig. 6). A medium size mesh of $408\times108 = 44{,}064$ cells is used for the baseline hump calculation as shown in Fig. 7. The boundary conditions (BCs)

set-up is illustrated in Fig. 8. The inlet is located at 6C upstream and the outlet is at 3C downstream of the hump. Total pressure, total temperature and flow angle are specified at the inlet as the boundary conditions. Static pressure is specified at the outlet boundary. The top wall is 0.9C away from the hump peak as designed in the experiments [61, 62]. Non-slip wall BC is enforced on all the walls. Details of mesh size are shown in Table 1.

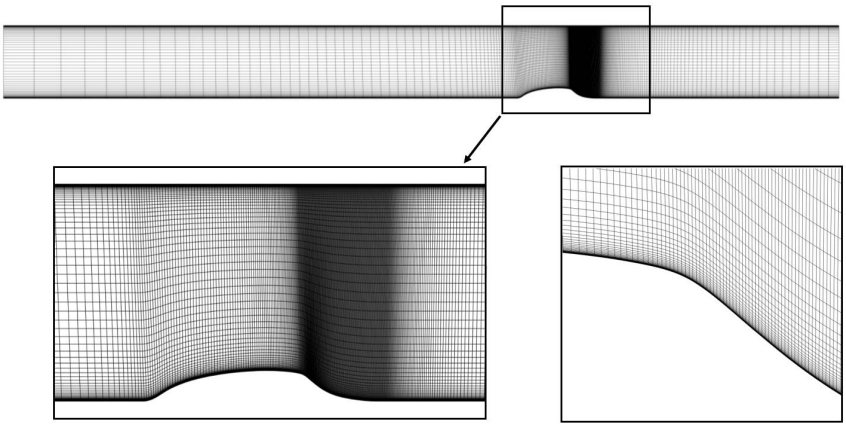

Figure 7: 2D computational mesh of baseline hump

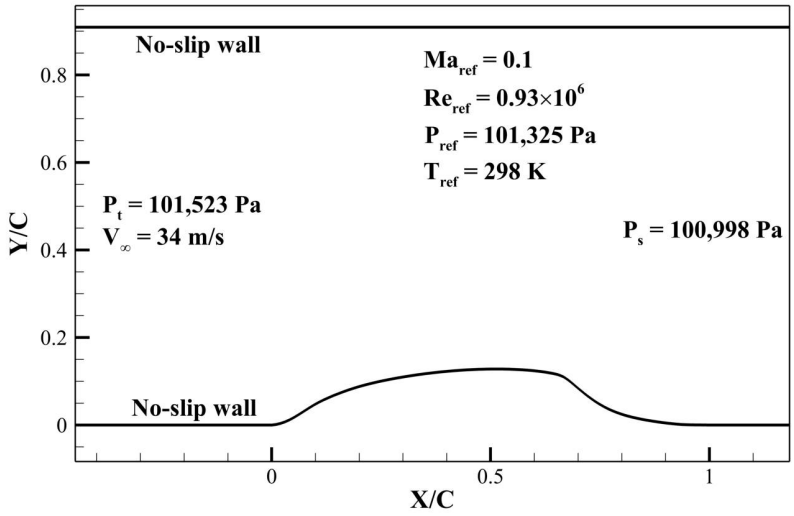

Figure 8: Boundary conditions of baseline hump simulation

Table 1: Details of the mesh sizes

Meshes	Hump	Injection duct	Suction plenum
Baseline	408×108	40×80	62×112
Refined	816×216	80×160	124×224

The unsteady simulation uses a constant non-dimensional characteristic time step $\Delta\bar{t} = 5\times10^{-3}$ with the maximum L2-norm residual typically reduced by 2 orders of magnitude within less than 40 pseudo time iterations per physical time step. Fig. 9 shows three typical convergence histories with time for three unsteady simulations, including a separated baseline flow and its associated mesh refinement, and an attached flow with flow control. The L2-Norm residual of the unsteady Navier-Stokes equations are basically driven to machine zero with 400 characteristic time, indicating the full convergence of the unsteady Navier-Stokes equations. All the cases in the present numerical study achieve the similar convergence, which ensures the reliability of the results.

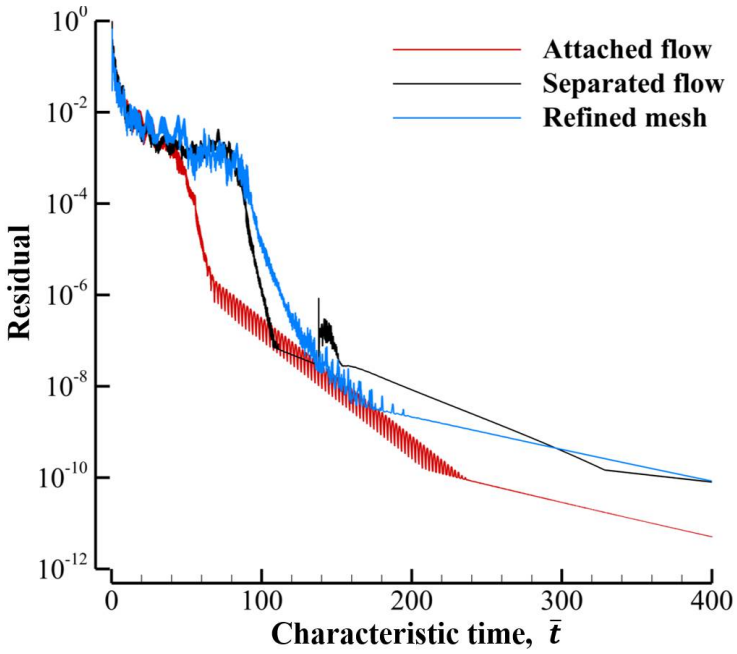

Figure 9: Convergence history of typical cases

3.5 Validations of Numerical Simulation

The experimental baseline hump, steady injection and suction cases [60, 62] are used to validate the simulation. All the location positions are measured from hump leading edge referring to Fig. 6 and Fig. 8. The blowing actuator is located at X/C = 0.68 and is angled at 10° to the freestream direction. For the suction only case, the hump geometry is the same as the injection only case with the injection slot replaced by a suction plenum located at X/C = 0.65 and the mesh is directly adopted from the NASA source [60].

In the experiment, the model was tested in a open-return wind tunnel with freestream velocity of U_{ref} = 34 m/s (Mach = 0.1). The Reynolds number for all the cases is 0.93×10^{6} based on the hump chord length. The CFD simulations use the same experimental Mach number and Reynolds number. Mesh refinement studies are also conducted by doubling the number of grid points in i, j direction simultaneously. The sizes of the baseline and refined meshes are given in Table 1.

Fig. 10 shows the Mach number contours of the baseline hump with the zoomed view of the velocity profile at the separation onset location. Fig. 11 compares the skin friction coefficient C_f and the pressure coefficient C_p with experimental data. The predicted C_f in Fig. 11 (a) indicates that the flow separation onset occurs at X/C = 0.663 ($\tau_w = 0$) and reattaches at X/C = 1.17, which agree well with the experi-

mental measurement with separation inception point at 0.665 and reattachment at 1.11 ± 0.003 [61, 63]. Downstream of the reattachment point beyond X/C= 1, the deviation between the predicted and experimental results is due to the massive flow separation. Similar discrepancy is reported in [60, 64]. Fig. 11 (b) is the predicted C_p distributions (in black) of the baseline hump compared with the experiment [61, 62]. Following the practice in [60, 65], the predicted time-averaged C_p distributions are shifted by -0.033 to match the experimental upstream reference conditions. As shown in Fig. 11 (b), the simulated C_p distributions of the baseline hump agree very well with experimental measurement, except the pressure drop at $0.6 < X/C < 0.9$ is slightly underestimated. Similar discrepancy is also reported by other researchers in [60, 65]. Fig. 11 (b) also indicates that both the pressure plateau starting point measured by the experiment and CFD simulation is located at 68.1%C, which is 1.8%C downstream of the separation onset point. This is because the pressure plateau is a response to the flow blockage creased by the separation. Thus the pressure plateau is usually a little downstream of the separation onset point. That is why it may be inaccurate that McGahan [30] used the pressure plateau as the separation onset point. The mesh refinement studies shown in Fig. 11 do not change the calculated results, indicating that the solutions achieve mesh independence. The computed pressure gradient distributions are also plotted in Fig.11 (b) for reference.

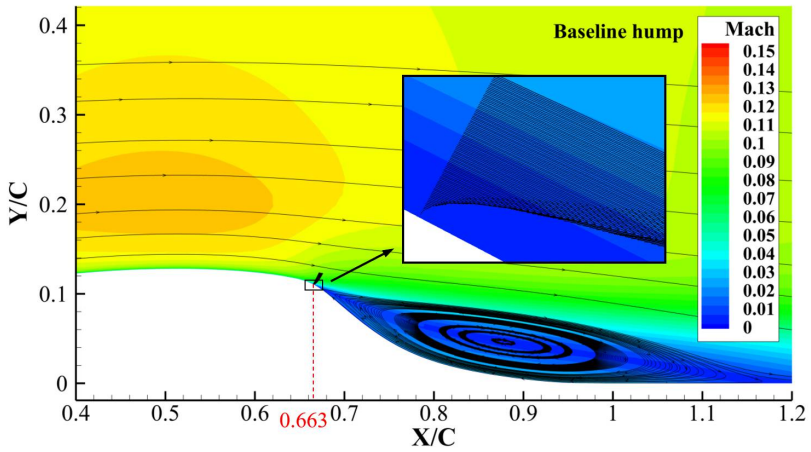

Figure 10: Mach number contour of the baseline hump

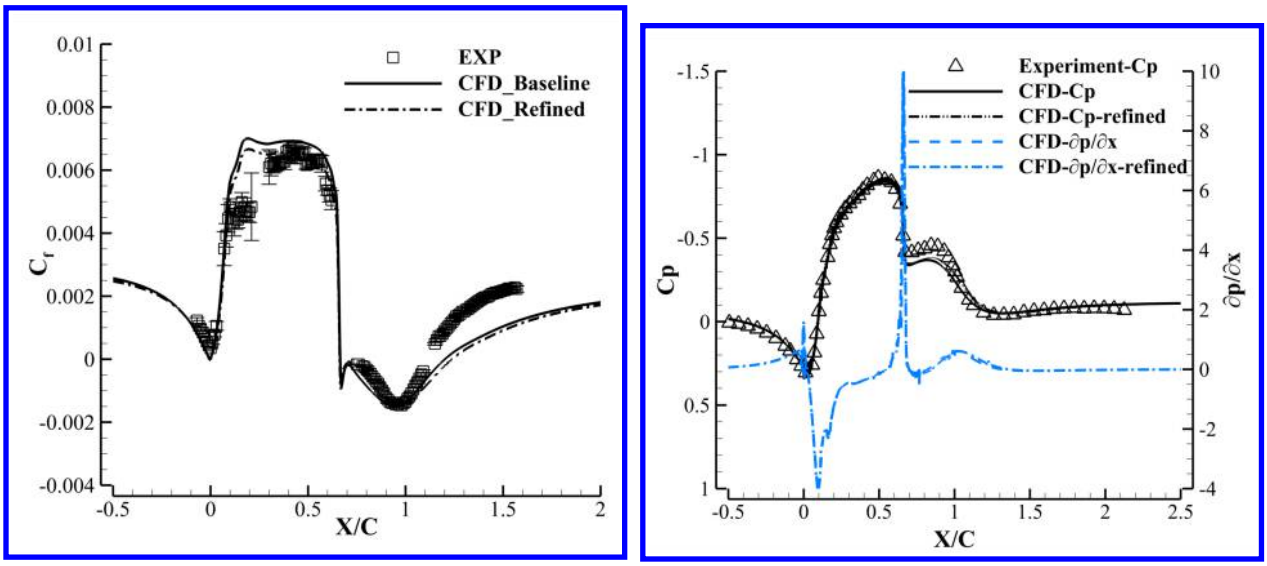

(a) Skin friction coefficient C_f (b) Pressure coefficient C_p

Figure 11: Comparison of the C_f and C_p distribution with experimental data

To further validate the numerical simulation, the hump cases with steady injection only and steady suction only are simulated and compared with the experiment respectively. Fig. 12 (a) is the Mach number contour of steady injection only with U_j=85 m/s used in the experiment [62]. The boundary conditions and case set-up are referred to [62, 66]. Steady blowing jet fully attaches the flow. The C_p distributions in Fig. 12 (b) shows that the predicted pressure distribution is again in very good agreement with the experiment [62]. The spike downstream of the low pressure suction peak is due to the jet injection. The solution is converged based on the mesh refinement as shown in Fig. 12 (b).

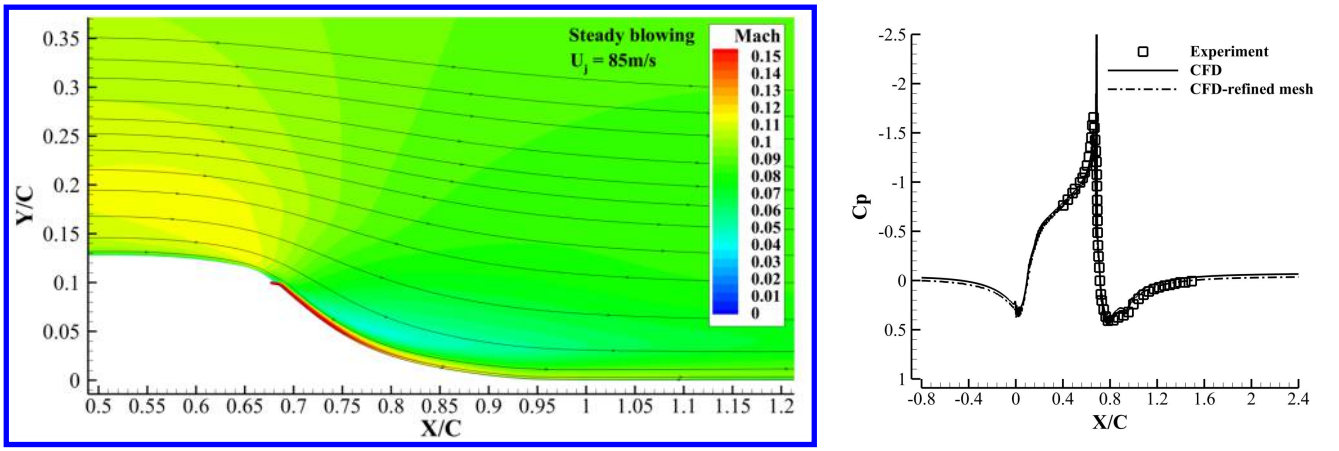

(a) Mach number contour (b) C_p distributions

Figure 12: CFD results of the hump with steady blowing

The last validation case is the one using steady suction only with C_μ of 0.241% (mass flow coefficient C_Q= 0.15% [67]). The computed Mach number contour in Fig. 13 indicates that the suction only flow control is not adequate to remove the flow separation, which is consistent with the experimental observation. The

predicted C_p distributions with mesh refinement are shown in Fig. 13. The CFD results are in good agreement with the experiment [60], but with the pressure rise under-predicted at $0.6 < \mathrm{X/C} < 1.2$, which indicates that the separation bubble thickness may be over-predicted. The similar discrepancy is observed in the URANS simulations conducted by other researchers [68, 69]. Further increase of the mesh size does not change the results as shown by the mesh refinement in Fig. 13 (b).

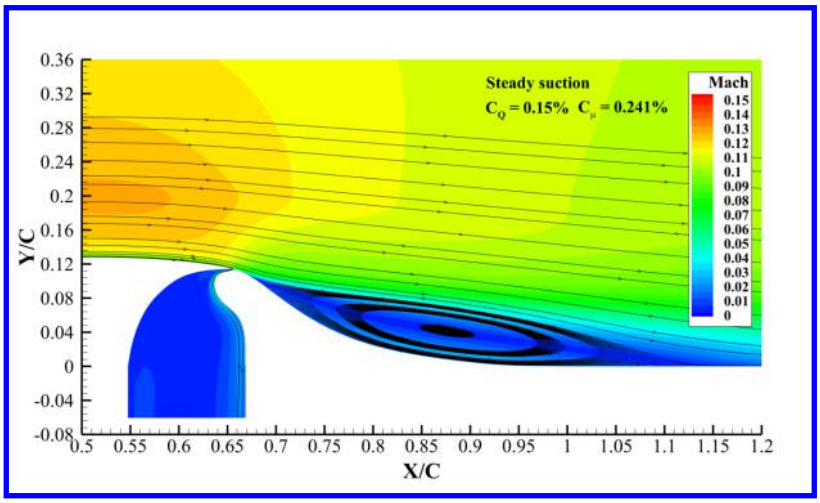

(a) Mach number contour

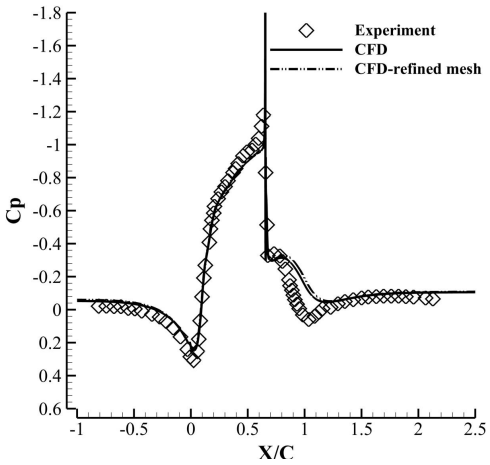

(b) C_p distributions

Figure 13: CFD results of the hump with steady suction

3.6 Co-flow Wall Jet Hump

3.6.1 CFWJ Hump Geometry

As sketched in Fig. 14, the CFWJ flow control is implemented by adding injection and suction slots at certain streamwise location on the baseline hump surface [61]. The surface between the injection and suction slots is slightly moved downward by 0.1%C to facilitate the tangential injection of the co-flow wall jet. Similar to a CFWJ airfoil, Fig. 14 (middle plot) shows that a small amount of mass flow is drawn into the hump downstream, pressurized and energized by a micro-compressor pumping system inside the hump, and ejected through the upstream injection slot tangential to the main flow. In the present simulation, the micro-compressor actuator is simulated by applying total pressure inlet BC at injection slot and static pressure outlet BC at suction slot as shown in the bottom of Fig. 14. This treatment of the injection and suction is thoroughly validated in the previous work [5, 7, 8, 10, 15, 16, 42, 54, 55, 56, 57, 58, 59, 70].

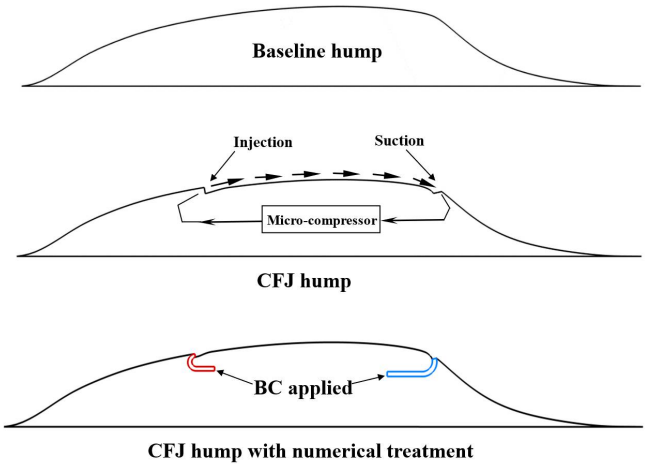

Figure 14: Sketches of the CFWJ hump

3.6.2 Numerical Results of CFWJ

Xu et al [12] conduct a trade study to optimize the injection and suction location with minimized energy expenditure. The two most efficient configurations of CFWJ hump consuming the least CFJ power are presented in this paper, CFWJ Case 2 and Case 9 as shown in Fig. 15. As indicated in the conclusions of wall jet momentum equation analysis of Section 2, applying the CFWJ flow control near separation onset point under adverse pressure gradient is the most effective, which is consistent with the practice of other researchers [60, 62]. This is shown in Case 2 with the injection at 67.5%C and Case 9 with the suction at 70%C. These two cases represent the CFWJ with injection dominant and suction dominant cases respectively by placing the injection or suction close to the baseline separation onset point, but both are slightly downstream of the onset point in the region of adverse pressure gradient [12]. The C_μ as defined in Eq. (20) is 0.85% for Case 2 and 0.77% for Case 9, which are the minimum C_μ to achieve full flow attachment for the two cases respectively [12].

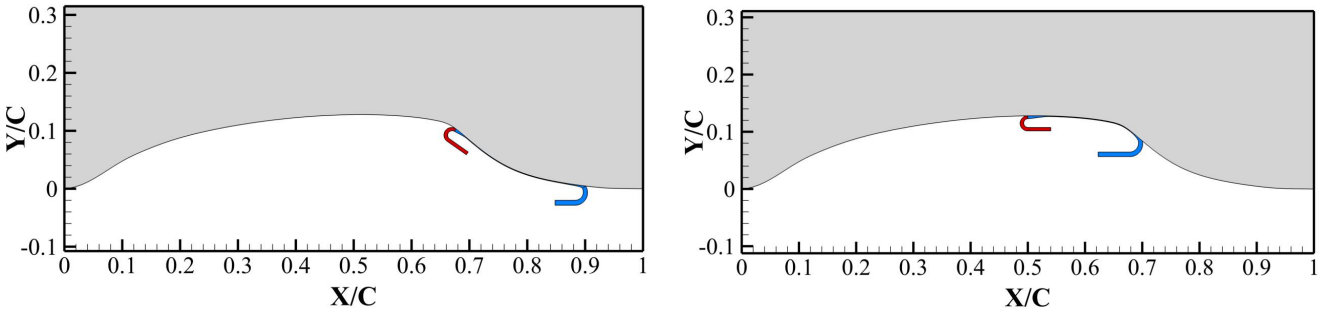

(a) CFWJ Case 2

(b) CFWJ Case 9

Figure 15: Configurations of the CFWJ NASA hump

$$C_\mu = \frac{\dot{m}V_j}{\frac{1}{2}\rho_{ref}{U_{ref}}^2 A_{ref}} \tag{20}$$

The CFWJ power required is defined by the total enthalpy rise from the suction duct outlet (compressor inlet) to the injection duct inlet (compressor outlet) [7]. The expression for power required (PR) and the non-dimensional power coefficient (P_c) are:

$$PR = \dot{m}H_{t2}(\Gamma^{\frac{\gamma-1}{\gamma}} - 1) \tag{21}$$

$$P_c = \frac{PR}{\frac{1}{2}\rho_{ref}U_{ref}^3 A_{ref}} \tag{22}$$

where, $\dot{m}$ is the CFWJ mass flow rate, H_{t2} is the total enthalpy at the suction slot, Γ is the total pressure ratio between the injection and suction, and γ is the specific heat ratio with a value of 1.4 for ideal gas.

3.7 CFWJ Case 2: Injection placed near separation onset point

Fig. 16 shows the spanwise vorticity contours and velocity profiles at five streamwise stations along the co-flow wall jet for CFWJ Case 2, which has the injection placed at 67.5%C location, slightly downstream of the separation onset point at 66.3%C. The velocity profile at Station 1 of upstream of the injection slot is a typical wall boundary layer profile, which is energized by the downstream CFWJ and would be nearly separated otherwise. The velocity profile at the Station 2 downstream of the injection slot shows a typical injection wall jet profile as sketched in Fig. 3 (b). Under the adverse pressure gradient, the wall jet profile becomes more smeared flowing downstream due to mixing with the mainstream as shown at Station 3 and 4. Further beyond the suction slot, the velocity profile returns to typical boundary layer profile but is energized as shown in Station 5. Fig. 16 also shows that the whole CFWJ is immersed in the APG region from the injection to the suction.

Away from the wall, the three counter-rotating layers of vorticity illustrated in Fig. 3 (b) are observed clearly downstream the injection slot in Fig. 16, a layer of clockwise vorticity due to the wall jet boundary layer in blue, a layer of counter clockwise vorticity due to the wall jet in red, a zero vorticity layer due to the wake from the injection slot lip in green, and a layer of clockwise vorticity due to the main flow boundary layer mixing with the wall jet in blue. With the CFWJ flowing to downstream, the wall jet counter clockwise vorticity layer is decayed and dissipated due to the mixing, and disappears downstream of the suction slot when the CFWJ ends.

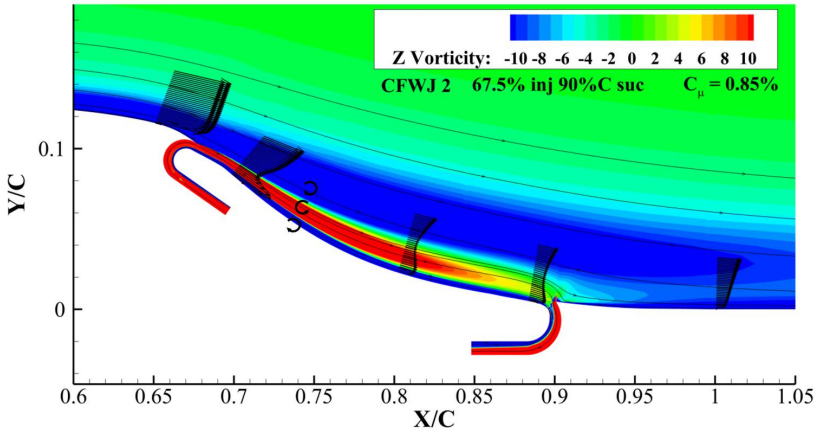

Figure 16: Spanwise vorticity and velocity profiles of the CFWJ Case 2

The pressure coefficient distributions along the wall in Fig. 17 indicates that the CFWJ Case 2 has the peak velocity much more augmented compared with the baseline due to the removal of flow separation. The injection near the baseline separation onset location is at the maximum APG region, which enhances the terms in the wall jet momentum equations to offset the APG.

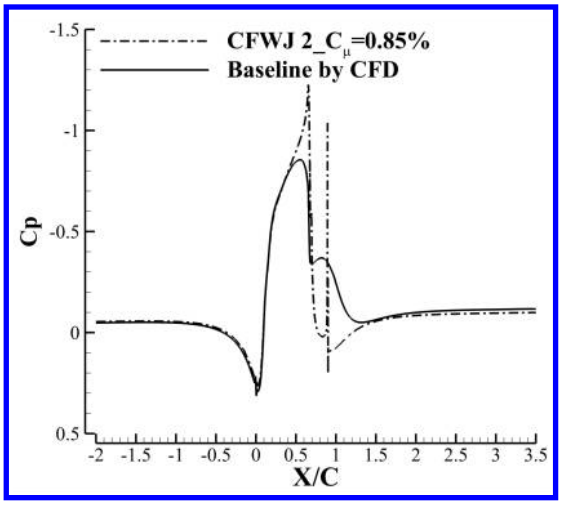

Figure 17: Surface Pressure coefficient distribution of Case 2

The boundary layer profiles of CFWJ Case 2 with the injection at 67.5%C are analyzed based on the wall jet differential Eq. (6) and integral Eq. (15) to investigate the injection effects. Fig. 18 (a) shows the transverse distributions of the terms in Eq. (6) normal and near the wall surface at the location 2%C downstream of the injection slot. The flow is attached at the location, which have the attached elevated velocity profiles with $\partial^2 u/\partial y^2 > 0$ ($LHS_D > 0$, Eq. (8)) on the wall due to the effect of the pressure gradient $\partial p/\partial x$ as indicated in Fig. 18.

Fig. 18 (a) shows that the LHS_D rapidly becomes negative when it is away from the wall to match the condition of a concave velocity profile of an attached flow. The profiles of the velocity and its slope are plotted in Fig. 18 (b) against the normal distance from the wall normalized by the injection slot height (D/h). Fig. 18 (b) demonstrates the typical attached elevated velocity profiles with the first order velocity

derivative $\partial u/\partial y$ increasing, which yields $\partial^2 u/\partial y^2 > 0$. The profiles in Fig. 18 are consistent with the analysis in Section 2. On the wall, the summation of the first three terms, R in Eq. (7) is basically zero. The local adverse pressure gradient is dominant on the wall and makes $\partial^2 u/\partial y^2 > 0$, but the flow is well attached.

Away from the wall, the adverse pressure gradient is offset by the rapidly increasing R of a negative value. Among the first three terms in Eq. (6), the turbulent diffusion $\partial u/\partial y \cdot \partial \mu/\partial y/Re$ makes the largest contribution to offset the adverse pressure gradient. This is attributed to the large gradient of the eddy viscosity and velocity (spanwise vorticity) of the wall jet injection, which transfers the momentum transversely to energize the boundary layer as analyzed in Section 1.2. Such effect may be insignificant for an adiabatic incompressible laminar wall jet since the viscosity coefficient gradient would be very small.

The second largest contribution to offset adverse pressure gradient is the streamwise inertia term $\rho u \cdot \partial u/\partial x$ exerted by the effects of CFWJ injection. The adverse pressure gradient increases the absolute value of $\partial u/\partial x$, which enhances the term $\rho u \cdot \partial u/\partial x$. The transverse convective term $\rho v \cdot \partial u/\partial y$ has a smaller magnitude for the wall jet injection.

The relations among the terms of the wall jet momentum Eq. (6) described above are clearly seen in Table 2 with the quantitative values of the Case 2 at y^+=2. The LHS_D already becomes negative at this location.

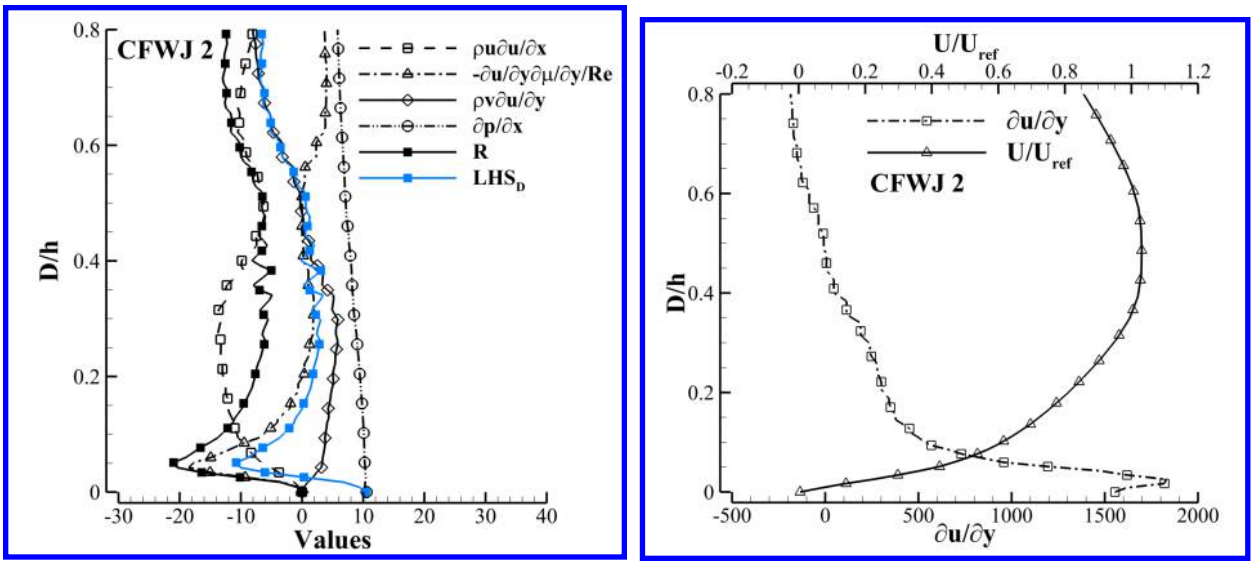

(a) Terms in Eq. (6) (b) Profiles of velocity and $\partial u/\partial y$

Figure 18: Distributions of different terms at 2%C downstream of the injection slot

Table 2: CFWJ Case 2, terms in Eq. (6) at y^+=2 at 2%C downstream of the injection slot

Cases	Location	C_μ	P_c	$\rho u \partial u/\partial x$	$\rho v \partial u/\partial y$	$-\partial u/\partial y \cdot \partial \mu/\partial y/Re$	$\partial p/\partial x$	LHS_D
CFWJ 2	69.5%C	0.85%	0.0030	-5.15	1.77	-18.54	10.33	-11.59

Table 3 presents the quantitative values of each term in wall jet integral Eq. (15). Term $\mathcal{S}$ is much larger than dp/dx and therefore keeps LHS_I value positive, indicating an attached flow with $\tau_w > 0$. The results

in Table 3 support the analysis in Section 2.4.

Table 3: CFWJ Case 2, terms in Eq. (15) at 2%C downstream of the injection slot

Cases	Location	C_μ	δ^*	θ	$d\theta/dx$	$\mathcal{Q}$	$\mathcal{S}$	dp/dx	LHS_I
CFWJ 2	69.5%C	0.85%	5.70×10^{-3}	3.97×10^{-3}	0.17	69.38	11.52	3.34	1.12×10^{-1}

The results in Fig. 18 and Tables 3 demonstrate an attached flow with $\partial^2 u/\partial y^2 > 0$ and $\tau_w > 0$, which is consistent with the separation control criterion suggested in the paper to achieve the attached flow with low energy expenditure.

3.8 CFWJ Case 9: Suction placed near separation onset point

Fig. 19 shows the vorticity contours of the CFWJ Case 9 with the suction slot placed near the separation onset point at 70%C in the region of adverse pressure gradient. The injection is located upstream of the suction in the region of favorable pressure gradient. In the CFWJ injection region, Fig. 19 indicates a wall jet velocity profile and 3 layers of counter-rotating vortex layers, which are thinner and shorter than those in Case 2 with adverse pressure gradient. The attached flow velocity profile in the diffusion region such as Station 5 is weaker than that of Case 2 at Station 3 in the similar location.

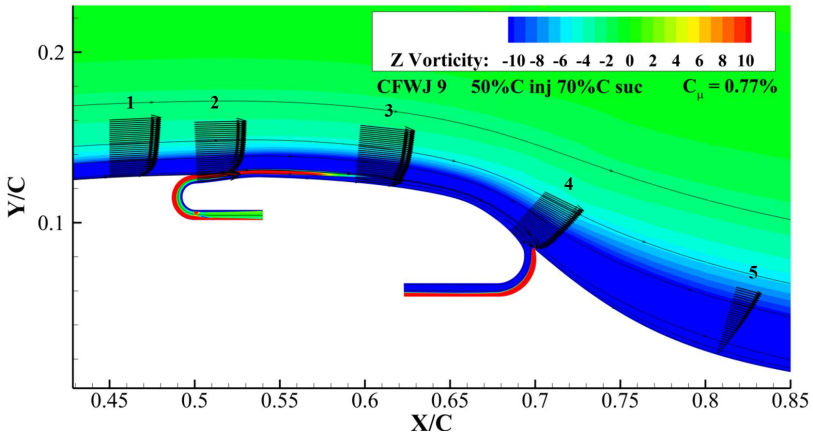

Figure 19: Spanwise vorticity and velocity profiles of the CFWJ Case 9

Similar to CFWJ Case 2, the pressure coefficient distributions along the wall in Fig. 20 indicates that the CFWJ Case 9 also has the peak velocity much more augmented compared with the baseline due to the removal of flow separation. The suction location near the separation onset is at the maximum APG region, which enhances the terms in the wall jet momentum equations to offset the APG.

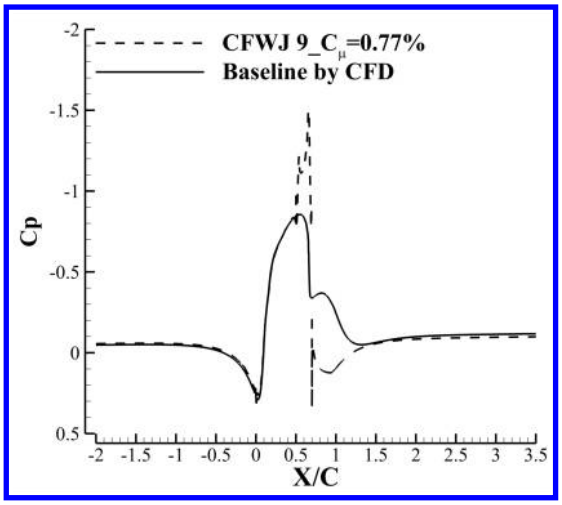

Figure 20: Surface Pressure coefficient distribution of Case 9

Fig. 21 is the profiles of the different terms of the wall jet momentum Eq. (6) for the CFWJ Case 9 to investigate the suction dominant effect of CFWJ. The profiles are plotted at 68.5%C location, 1.5%C upstream of the suction slots. LHS_D again begins with a positive value at the wall due to the effect of adverse pressure gradient, indicating that the flow is at the attached elevated state with $\partial^2 u/\partial y^2 > 0$. Away from the wall, the LHS_D rapidly turns to negative to match the attached flow concave velocity profile. The quantitative contributions near the wall with y^+=2 are listed in Table 4. The dominant term offsetting the adverse pressure gradient for this case is again the turbulent diffusion term $\partial u/\partial y \cdot \partial \mu/\partial y/Re$ as shown in Fig. 21 and Table 4. This is attributed to the streamwise suction that creates an acceleration within the boundary layer with increased transverse velocity gradient, or wall spanwise vorticity. The transverse convection term $\rho v \cdot \partial u/\partial y$, or the wall vortex flux, has a much larger contribution to offset the APG than the injection dominant Case 2, which is benefited from the negative vertical velocity component entering to the wall due to the suction and the high spanwise vorticity that the suction induces.

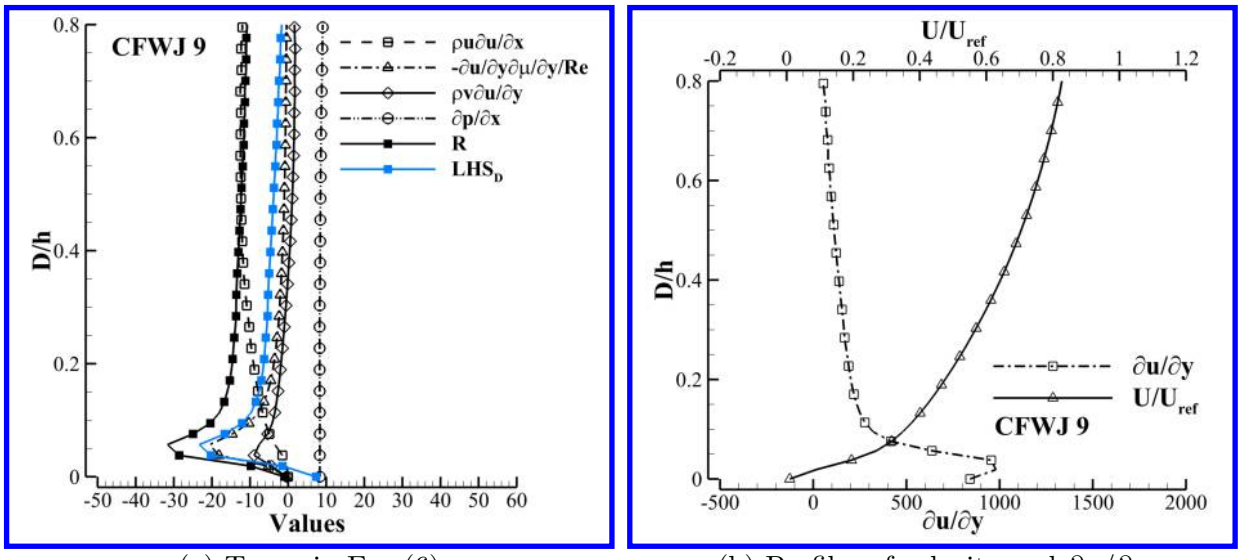

(a) Terms in Eq. (6) (b) Profiles of velocity and $\partial u/\partial y$

Figure 21: Distributions of different terms at 1.5%C upstream of the suction slot

Table 4: CFWJ Case 9, terms in Eq. (6) at y^+=2 at 1.5%C upstream of the suction slot

Cases	Location	C_μ	P_c	$\rho u\partial u/\partial x$	$\rho v\partial u/\partial y$	$-\partial u/\partial y \cdot \partial\mu/\partial y/Re$	$\partial p/\partial x$	LHS_D
CFWJ 9	68.5%C	0.77%	0.0032	-1.53	-8.91	-18.16	8.31	-20.29

As shown in Fig. 19 and 20, because the suction slot of Case 9 is placed near the separation onset, the injection has to be placed upstream in the FPG region. Only a small portion of the CFWJ near the suction slot is in APG. The Case 9 is the optimum configuration with the minimum CFWJ energy expenditure from the trade study with several injection locations upstream. Comparing the CFJ power coefficient P_c in Table 2 and Table 4, both CFWJ Case 2 and Case 9 require a very small power consumption to remove the flow separation. This is attributed to the proposed separation control criterion to attach the flow with $\partial^2 u/\partial y^2 > 0$ and $\tau_w > 0$. However, the P_c of Case 9 is about 6.7% higher than that of Case 2. It does indicate that the CFWJ is more favorable to work in full adverse pressure gradients as in Case 2.

A numerical experiment is attempted to achieve $\partial^2 u/\partial y^2 < 0$ following the previous guideline of Gad-el-Hak and Bushnell [1] for the Case 2. The $\partial^2 u/\partial y^2$ remains positive even with CFWJ power coefficient P_c increased by 16 times. The effort to achieve $\partial^2 u/\partial y^2 < 0$ is then given up. This numerical experiment supports the conclusion that $\partial u^2/\partial y^2 < 0$ at the wall for separation control is unnecessary, excessive for energy expenditure, and may not be achievable.

Table 5 compares the values of each term of the integral form momentum Eq. (15) for CFWJ Case 9. The measured location is the same as that for the differential momentum equation in Table 4. The streamwise suction substantially thins the boundary layer than the Case 2 with δ^* and θ reduced more than 50%, which indicates a more energized boundary layer upstream of the suction slot due to the stronger turbulent diffusion and mixing induced by the streamwise suction as shown in Fig. 21 and Table 4. With the reduced δ^* and θ, the compound factor $\mathcal{S}$ in Eq. (15) is substantially increased to offset the adverse pressure gradient and attach the flow. Overall, both the two CFWJ cases have sufficient $\mathcal{S}$ factor to offset the adverse pressure gradient and make the sign of LHS_I, i.e., the wall shear stress, positive with attached flow.

Table 5: CFWJ Case 9, terms in Eq. (15) at 1.5%C upstream of the suction slot

Cases	Location	C_μ	δ^*	θ	$d\theta/dx$	$\mathcal{Q}$	$\mathcal{S}$	dp/dx	LHS_I
CFWJ 9	68.5%C	0.77%	2.02×10^{-3}	1.21×10^{-3}	0.12	211.33	25.30	7.22	8.03×10^{-2}

4 Conclusions

The wall jet momentum equations in both the differential form and integral form are analyzed to provide a separation control criterion and a guideline to investigate the separation control mechanism of CFWJ. The followings are some conclusions obtained from wall jet momentum equations analysis and the URANS numerical investigations on the NASA hump:

1. The previous guideline to obtain negative $\partial u^2/\partial y^2$ at the wall for separation control is unnecessary, excessive for energy expenditure, and may not be achievable. This is because $\partial u^2/\partial y^2 > 0$ is necessary

in adverse pressure gradients at the wall regardless the flow is separated or attached. The $\partial u^2/\partial y^2$ is positive at the wall for all the flows attached by the CFWJ based on the URANS simulation. It rapidly becomes negative away from the wall due to co-flow wall jet effect of offsetting the adverse pressure gradient. A numerical experiment with CFWJ power coefficient increased by 16 times is still not able to achieve an attached flow with $\partial u^2/\partial y^2 < 0$.

2. A more energy efficient separation control criterion is to seek an attached elevated flow with $\tau_w > 0$ and $\partial u^2/\partial y^2 \geq 0$.

3. Turbulent diffusion near the wall is the most dominant term to offset adverse pressure gradient for both the CFWJ injection and suction. It plays a key role for wall jet mixing and energizing the wall boundary layer.

4. For the CFWJ injection, keeping the injection tangential to the wall surface is most effective to minimize flow blockage, maximize the spanwise vorticity, turbulent diffusion, and streamwise inertia force term in order to offset the adverse pressure gradient.

5. For CFWJ suction, a streamwise suction not only enhances those same terms by the injection, but also augments the wall vorticity flux due to the velocity component pointing to the wall.

6. The CFWJ injection has a typical wall jet velocity profile with three counter rotating vortex layers. The suction does not create the counter rotating vortex layers. The suction energizes the upstream boundary layer via convection terms and turbulent diffusion.

7. Adverse pressure gradients benefit CFWJ to be more effective and efficient.

8. It is most effective to apply flow control near the separation onset point because it may have the highest APG that enhances the CFWJ effect. It may also have the lowest static pressure to make it easier to create a spanwise vorticity and mass flux than in a deep separation region.

9. It is more efficient and effective to place the CFWJ injection near the separation onset point and the suction downstream. This will immerse the entire CFWJ in the APG region to enhance the CFWJ effect. It is more efficient to eject the flow to a low pressure location and withdraw the flow from a high pressure region. This conclusion is demonstrated by comparing the two numerically simulated CFWJ hump cases.

10. The CFWJ has the mechanism to grow its control capability with the increasing adverse pressure gradient. When the APG grows, all the terms offsetting the APG also grow, provided that the CFWJ has the sufficient clockwise spanwise vorticity and mass flow at the wall established as the essential condition. This may provide CFWJ the ability to suppress flow separation in very severe adverse pressure gradients.

5 Acknowledgment

We are very grateful to Dr. Kenneth Coles for permitting us to quote the wall jet integral equation derivation from the book of the late Prof. Donald Coles. We would also like to thank Dr. Meng Wang at the University of Notre Dame for his very helpful discussion. The authors would like to acknowledge the computing resource provided by the Center of Computational Sciences at the University of Miami.

Disclosure: The University of Miami and Dr. Gecheng Zha may receive royalties for future commercialization of the intellectual property used in this study. The University of Miami is also equity owner in CoFlow Jet, LLC, licensee of the intellectual property used in this study.

Appendix: Integral Form of Turbulent Wall Jet Momentum Equation

With the approval of the heirs of Prof. Donald Coles, the Coles' derivation [43] of the integral form of turbulent wall jet momentum equation is presented herein.

The incompressible wall jet momentum equation of Eq. (4) is repeated here as below:

$$\rho u\frac{\partial u}{\partial x}+\rho v\frac{\partial u}{\partial y}+\frac{\partial p}{\partial x}=\frac{\partial \tau_{xy}}{\partial y} \tag{23}$$

The freestream Euler equation relates the pressure gradient with convention term as:

$$\rho u_\infty\frac{du_\infty}{dx}=-\frac{dp}{dx} \tag{24}$$

The incompressible continuity equation gives:

$$\frac{\partial u}{\partial x}+\frac{\partial v}{\partial y}=0 \tag{25}$$

Combining Eq. (24) and (25) with Eq. (23) yields:

$$\rho(\frac{\partial u^2}{\partial x}+\frac{\partial uv}{\partial y})=\rho u_\infty\frac{du_\infty}{dx}+\frac{\partial \tau_{xy}}{\partial y} \tag{26}$$

Integrate Eq. (26) normal to the wall from y=0 $\rightarrow$ y, with the boundary condition $v=0$ at $y=0$.

$$\rho\int_0^y\frac{\partial u^2}{\partial x}dy+\rho\int_0^y\frac{\partial uv}{\partial y}dy=\rho\int_0^y u_\infty\frac{du_\infty}{dx}dy+\int_0^y\frac{\partial \tau_{xy}}{\partial y}dy \tag{27}$$

Then,

$$\rho\int_0^y\frac{\partial u^2}{\partial x}dy+\rho uv=\rho\frac{du_\infty}{dx}\int_0^y u_\infty dy+\tau_{xy}-\tau_w \tag{28}$$

or

$$\rho\int_0^y\frac{\partial u^2}{\partial x}dy+\rho u\int_0^y\frac{\partial v}{\partial y}dy=\rho\frac{du_\infty}{dx}\int_0^y u_\infty dy+\tau_{xy}-\tau_w \tag{29}$$

Integrating the continuity equation Eq.(25) and substituting it to Eq.(29) gives,

$$\rho \int_0^y \frac{\partial u^2}{\partial x} dy - \rho u \int_0^y \frac{\partial u}{\partial x} dy - \rho \frac{du_\infty}{dx} \int_0^y u_\infty dy - \tau_{xy} + \tau_w = 0 \tag{30}$$

Use the following relation:

$$-\rho \frac{\partial u u_\infty}{\partial x} + \rho u_\infty \frac{\partial u}{\partial x} + \rho u \frac{du_\infty}{dx} = 0 \tag{31}$$

Integrating Eq.(31) and combining it with Eq.(30) yields:

$$\rho \frac{\partial}{\partial x} \int_0^y (u^2 - u u_\infty) dy + \rho (u_\infty - u) \int_0^y \frac{\partial u}{\partial x} dy + \rho \frac{du_\infty}{dx} \int_0^y (u - u_\infty) dy - \tau_{xy} + \tau_w = 0 \tag{32}$$

Let y $\to \infty$, then $\tau_{xy} \to 0$, $u \to u_\infty$. Eq. (32) becomes:

$$\rho \frac{d}{dx} \int_0^\infty u(u_\infty - u) dy + \rho \frac{du_\infty}{dx} \int_0^\infty (u_\infty - u) dy - \tau_w = 0 \tag{33}$$

This is the momentum-integral equation of Karmann. Use the definition of displacement thickness δ^*:

$$u_\infty \delta^* = \int_0^\infty (u_\infty - u) dy \tag{34}$$

and momentum thickness θ:

$$u_\infty^2 \theta = \int_0^\infty u(u_\infty - u) dy \tag{35}$$

Eq. (33) becomes:

$$\tau_w = \rho \frac{d}{dx} u_\infty^2 \theta + \rho u_\infty \delta^* \frac{du_\infty}{dx} \tag{36}$$

This is the turbulent wall jet integral momentum equation given by Coles [43].

References

[1] Gad-el-Hak, M., *Flow Control, Passive, Active, and Reactive Flow Management.* Cambridge University Press, 2000, DOI: 10.1017/CBO9780511529535.

[2] Prandtl, L. , "*Ü*ber fl*ü*ssigkeitsbewegung bei sehr kleiner reibugn." in Proc. Third Int. Math. Cong. pp. 484-491, Heidelberg, Germany, 1904.

[3] Gad-el-Hak, M. and Sushnell, D. M., "Separation Control: Review," *Journal of Fluids Engineering*, vol. 113, pp. 5–30, 1991, DOI: 10.1115/1.2926497.

[4] Schlichting H. and Gersten K., *Boundary-Layer Theory*. Berlin: Springer–Verlag, 8th ed., 2001, DOI: 10.1007/978-3-662-52919-5.

[5] Zha, G.-C and Paxton, C. and Conley, A. and Wells, A. and Carroll, B., "Effect of Injection Slot Size on High Performance Co-Flow Jet Airfoil," *AIAA Journal of Aircraft*, vol. 43, 2006, DOI: 10.2514/1.16999.

[6] Zha, G.-C and Carroll, B. and Paxton, C. and Conley, A. and Wells, A., "High Performance Airfoil using Co-Flow Jet Flow Control," *AIAA Journal*, vol. 45, 2007, DOI: DOI: 10.2514/1.20926.

[7] Lefebvre, A. and Dano, B. and Bartow, W. and Di Franzo, M. and Zha, G.-C., "Performance and Energy Expenditure of Co-Flow Jet Airfoil with Variation of Mach Number," *AIAA Journal of Aircraft*, vol. 53, pp. 1757–1767, 2016, DOI: 10.2514/1.C033113.

[8] Yang, Y.-C. and Zha, G.-C., "Super-Lift Coefficient of Active Flow Control Airfoil: What Is the Limit?." AIAA Paper 2017-1693, AIAA SCITECH2017, 55th AIAA Aerospace Science Meeting, Grapevine, Texas, 9-13 January 2017, DOI: 10.2514/6.2017-1693.

[9] Zha G. and Yang Y. and Ren Y. and McBreen B., "Super-lift and Thrusting Airfoil of Coflow Jet Actuated by Micro-compressors," in *2018 Flow Control Conference*, p. 3061, AIAA Paper 2017-3061, 2018, DOI: 10.2514/6.2018-3061.

[10] Xu K.and Zha G., "High Control Authority 3D Aircraft Control Surfaces Using Co-Flow Jet." AIAA Journal of Aircraft (2020), accessed July 14, 2020. DOI: 10.2514/1.C035727, 2020.

[11] Xu K. and Ren Y. and Zha G., "Numerical Investigation of NASA Hump Using Co-flow Jet for Separation Control," in *AIAA Scitech 2020 Forum, AIAA 2020-1058*, p. 1058, 2020, DOI: 10.2514/6.2020-1058.

[12] Xu K. and Ren Y. and Zha G., "Numerical Analysis of Energy Expenditure for Co-Flow Wall Jet Separation Control." Proceedings of AIAA 2022 SCITECH, San Diego, CA., January 2022.

[13] Xu K. and Zha G., "Mitigation of serpentine duct flow distortion using coflow jet active flow control," in *AIAA AVIATION 2020 FORUM,VIRTUAL EVENT, AIAA 2020-2954*, June 15-19, 2020, DOI: 10.2514/6.2020-2954.

[14] Xu K. and Zha G., "Distortion Elimination for Serpentine Inlet Using CoFlow Jet Flow Control with Variation of Mach Numbers," in *AIAA Propulsion and Energy 2020 Forum, AIAA 2020-3775*, p. 3775, 2020, DOI: 10.2514/6.2020-3775.

[15] Zha G., Gao W. and Paxton C.D., "Jet Effects on Co-Flow Jet Airfoil Performance." AIAA Journal, Volum 45, pp 1222–1231, 2007, DOI: 10.2514/1.23995.

[16] Wang, B.-Y. and Haddoukessouni, B. and Levy, J. and Zha, G.-C., "Numerical Investigations of Injection Slot Size Effect on the Performance of Co-Flow Jet Airfoil," *Journal of Aircraft*, 2008, DOI: 10.2514/1.37441.

[17] Launder, B. E. and Rodi, W. , "The Turbulent Wall Jet - Measurement and Modeling," *Journal of Fluid Mechanics*, vol. 15, pp. 429–59, 1983, DOI: 10.1146/annurev.fl.15.010183.002241.

[18] Irwin, H. P. A., "Measurement in a Self-preserving Plane Wall Jet in a Positive Pressure Gradient," *Journal of Fluid Mechanics*, vol. 61, pp. 33–63, 1973, DOI: 10.1017/S0022112073000558.

[19] Englar, R. J. , "Circulation Control for High Lift and Drag Generation on STOL Aircraft," *Journal of Aircraft*, vol. 12, pp. 457–463, 1975, DOI: 10.2514/3.59824.

[20] Englar, R. J., "Circulation Control Pneumatic Aerodynamics: Blown Force and Moment Augmentation and Modifications; Past, Present and Future." AIAA 2000-2541, June 2000, DOI: 10.2514/6.2000-2541.

[21] Jones, G. S., "Pneumatic Flap Performance for a 2D Circulation Control Airfoil, Stedy & Pulsed." *Applications of Circulation Control Technologies*, Chapter 7, p. 191-244, Vol. 214, Progress in Astronautics and Aeronautics, AIAA Book Series, Editors: Joslin, R. D. and Jones, G. S., 2006, DOI: 10.2514/4.866838.

[22] Wang Y. and Zha G.-C. , "Study of 3D Co-flow Jet Wing Induced Drag and Power Consumption at Cruise Conditions." AIAA Paper 2019-0034, AIAA SciTech 2019, San Diego, CA, January 7-11, 2019, DOI: 10.2514/6.2019-0034.

[23] Sleeman, W. C. Jr. and Hohlweg, W. C. , "Low-Speed Wind Tunnel Investigation of a Four Engine Upper Surface Blown Model having a Swept Wing and Rectangular and D-Shaped Exhaust Nozzle." NASA TN D-8061, Dec. 1975.

[24] SUSSMAN, M., REED, J., and OKEEFE, J. , "USB Environment Assessment Based on YC-14 Flight Test Measurement." AIAA Paper 77-0593, Nov. 1981, DOI: 10.2514/6.1977-593.

[25] Riddle, D. W. and Innis, R. C. and Martin, J. L. and Cochrane, J. A. , "Powered-Lift takeoff performance characteristics determined from flight test of the Quiet Short-Haul Research Aircraft /QSRA/." AIAA Paper 81-2409, AIAA Flight Testing Conference, Las Vegas, NV, Nov. 1981, DOI: 10.2514/6.1981-2409.

[26] Wimpress, J. K. and Newberry, C. F. , "The YC-14 STOL Prototype: Its Design, Development and Flight Test." AIAA Case Study, AIAA, Reston, 1998, DOI: 10.2514/4.868337.

[27] Forthmann, E., "Turbulent Jet Expansion ." NACA TM-789, March 1936.

[28] Glauert, M. B., "The Wall Jet," *Journal of Fluid Mechanics*, pp. 625–643, 1956, DOI: 10.1017/S002211205600041X.

[29] Bradshaw, P. and Gee, M. T. , "Turbulent Wall Jets with and without an External Stream." Aero. Res. Counc. R. & M. 3252, 1960.

[30] McGahan, W. A., "The Incompressible, Turbulent Wall Jet in an Adverse Pressure Gradient." MIT Rep. No. 82, 1965.

[31] Newman, B. G., "The Prediction of Turbulent Jets and Wall Jet," *Canadian Aeronautics and Space Journal*, vol. 15, 1969.

[32] Patel, R. P. and Newman, B. G. , "Self-prserving, two-dimensional turbulent jets and wall jets in a moving stream." Mech. Engng Res. Lab, McGill University, Rep. AE 5., 1961.

[33] Neuendorf, R. and Wygnanski, I., "On a Turbulent Wall Jet Flowing over a Circular Cylinder," *Journal of Fluid Mechanics*, vol. 381, pp. 1–25, 1999, DOI: 10.1017/S0022112098003668.

[34] Zhou, M.D. and Heine, C. and Wygnanski, I., "The Effects of Excitation on the Coherent and Random in a Plane Wall Jet," *Journal of Fluid Mechanics*, vol. 242, 1992, DOI: 10.1017/S0022112096001711.

[35] Katz, Y. and Horev, E. and Wygnanski, I., "The Forced Turbulent Wall Jet," *Journal of Fluid Mechanics*, vol. 242, pp. 557–609, 1992, DOI: 10.1017/S0022112092002507.

[36] Yang, Y.-C. and Zha, G.-C., "Super Lift Coefficient of Cylinder Using Co-Flow Jet Active Flow Control." AIAA Paper 2018-0329, AIAA SciTech Forum, 2018 AIAA Aerospace Sciences Meeting, Kissimmee, FL, 8-12 January 2018.

[37] Yang, Y.-C. and Zha, G.-C., "Numerical Investigation of Ultra-High Lift Coefficient Co-Flow Jet Wing Without Flaps." AIAA Paper 2018-2054, AIAA SciTech Forum, 2018 AIAA Aerospace Sciences Meeting, Kissimmee, FL, 8-12 January 2018.

[38] Smith, A.M.O., "High-Lift Aerodynamics," *Journal of Aircraft*, vol. 12, pp. 501–530, 1975.

[39] Wiedemann, J. and Gersten, K. , "Drag Reduction due to Boundary-layer Control by Combined Blowing and Suction," tech. rep., AGARD-CP-365, 14-1 to 14-10, 1984.

[40] Abernathy F. H., *Fundamentals of boundary layers*. Encyclopaedia Britannica educational Corporation [SD]!, 1968.

[41] Greitzer E. M., Tan C. S. and Graf M. B., *Internal Flow: Concepts and Applications*. Cambridge University Press, 2004, DOI: 10.1017/CBO9780511616709.

[42] Liu, Z.-X. and Zha, G.-C., "Transonic Airfoil Performance Enhancement Using Co-Flow Jet Active Flow Control." AIAA Paper 2016-3066, AIAA Aviation, June 13-17 2016, DOI: 10.2514/6.2016-3472.

[43] Coles, D. , *Topics in Shear Flow*. DOI: 10.7907/Z90P0X7D: Unpublished, 2017.

[44] Spalart, P.R. and Allmaras, S.R. , "A One-equation Turbulence Model for Aerodynamic Flows." AIAA-92-0439, 30th Aerospace Sciences Meeting and Exhibit, Reno,NV,U.S.A., 06 January 1992 - 09 January 1992, DOI: 10.2514/6.1992-439.

[45] Shen, Y.-Q. and Zha, G.-C., " Improved Seventh-Order WENO Scheme ." AIAA Paper 2010-1451, 48th AIAA Aerospace Sciences Meeting, Orlando, FL, Jan. 4-6, 2010, DOI: 10.2514/6.2010-1451.

[46] Zha, G.-C. and Shen, Y. and Wang, B., "An improved low diffusion E-CUSP upwind scheme ," *Journal of Computer & Fluids*, vol. 48, pp. 214–220, 2011, DOI: 10.1016/j.compfluid.2011.03.012.

[47] Shen, Y.-Q. and Zha, G.-C. and Wang, B.-Y., "Improvement of Stability and Accuracy for Weighted Essentially Nonoscillatory Scheme," *AIAA Journal*, vol. 47, pp. 331–344, 2009, DOI: 10.2514/1.37697.

[48] Shen, Y.-Q. and Zha, G.-C. and Chen, X.-Y., " High Order Conservative Differencing for Viscous Terms and the Application to Vortex-Induced Vibration Flows," *Journal of Computational Physics*, vol. 228(2), pp. 8283–8300, 2009. DOI: 10.1016/j.jcp.2009.08.004.

[49] Shen, Y.-Q. and Zha, G.-C. , " Improvement of the WENO Scheme Smoothness Estimator," *International Journal for Numerical Methods in Fluids*, vol. 64, 2010, DOI: 10.1002/fld.2186.

[50] Zha, G-C and Bilgen, E, "Numerical Study of Three-dimensional Flows Using Unfactored Upwind-relaxation Sweeping Algorithm," *Journal of Computational Physics*, vol. 125, no. 2, pp. 425–433, 1996, DOI: 10.1006/jcph.1996.0104.

[51] Zha, G.-C. and Bilgen, E., "Numerical Solutions of Euler Equations by Using a New Flux Vector Splitting Scheme ," *International Journal for Numerical Methods in Fluids*, vol. 17, pp. 115–144, 1993, DOI: 10.1002/fld.1650170203.

[52] Chen X. and Zha G., "Fully coupled fluid–structural interactions using an efficient high resolution upwind scheme," *Journal of Fluids and Structures*, vol. 20, no. 8, pp. 1105–1125, 2005, DOI: 10.1016/j.jfluidstructs.2005.02.011.

[53] Wang, B.-Y. and Zha, G.-C. , "A General Sub-Domain Boundary Mapping Procedure For Structured Grid CFD Parallel Computation," *AIAA Journal of Aerospace Computing, Information, and Communication*, vol. 5, No.11, pp. 2084–2091, 2008, DOI: 10.2514/1.35498.

[54] Zha G., Carroll B.F., Paxton C.D., Conley C.A. and Wells A., "High-performance Airfoil Using Coflow Jet Flow Control," *AIAA journal*, vol. 45, no. 8, pp. 2087–2090, 2007, DOI: 10.2514/1.20926.

[55] Lefebvre A., Dano B., Bartow W.B., Fronzo M.D. and Zha G., "Performance and Energy Expenditure of Coflow Jet Airfoil with Variation of Mach Number," *Journal of Aircraft*, vol. 53, no. 6, pp. 1757–1767, 2016, DOI: 10.2514/1.C033113.

[56] Dano, B. P. E., Kirk, D. and Zha, G.-C., "Experimental Investigation of Jet Mixing Mechanism of Co-flow Jet Airfoil." AIAA-2010-4421, (5th AIAA Flow Control Conference, Chicago, IL), 28 Jun - 1 Jul 2010, DOI: 10.2514/6.2010-4421.

[57] Dano B. P. E., Zha G.-C. and Castillo M., "Experimental Study of Co-Flow Jet Airfoil Performance Enhancement Using Micro Discreet Jets." AIAA Paper 2011-0941, 49th AIAA Aerospace Sciences Meeting, Orlando, FL,, 4-7 January 2011, DOI: 10.2514/6.2011-941.

[58] Lefebvre, A. and Zha, G.-C. , "Design of High Wing Loading Compact Electric Airplane Utilizing Co-Flow Jet Flow Control." AIAA Paper 2015-0772, AIAA SciTech2015: 53nd Aerospace Sciences Meeting, Kissimmee, FL, 5-9 Jan 2015, DOI: 10.2514/6.2015-0772.

[59] Lefebvre, A. and Zha, G.-C., "Trade Study of 3D Co-Flow Jet Wing for Cruise Performance." AIAA Paper 2016-0570, AIAA SCITECH2016, AIAA Aerospace Science Meeting, San Diego, CA, 4-8 January 2016, DOI: 10.2514/6.2016-0570.

[60] Rumsey C, "2DWMH: 2D NASA Wall-Mounted Hump Separated Flow Validation Case." Turbulence Modeling Resource, turbmodels.larc.nasa.gov, 2003.

[61] Greenblatt D., Paschal K.B., Yao C.S., Harris J., Schaeffler N.W. and Washburn A.E., "Experimental Investigation of Separation Control Part 1: Baseline and Steady Suction," *AIAA journal*, vol. 44, no. 12, pp. 2820–2830, 2006, DOI: 514/1.13817.

[62] Borgmann, D., Pande, A., Little, J. and Woszidlo, R. , "Experimental Study of Discrete Jet Forcing for Flow Separation Control on a Wall Mounted Hump." AIAA Paper 2017-1450, AIAA SciTech 2017, 55th AIAA Aerospace Sciences Meeting, Grapevine, Texas, January 2017, DOI: 10.2514/6.2017-1450.

[63] Fisher R., Nishino T. and Savill M., "Numerical Analysis of a Bidirectional Synthetic Jet for Active Flow Control," *AIAA Journal*, vol. 55, no. 3, pp. 1064–1069, 2017, DOI: 10.2514/1.J055081.

[64] Naughton, J. W., Viken, S., Greenblatt, D., "Skin Friction Measurements on the NASA Hump Model," *AIAA journal, DOI: 10.2514/1.14192*, vol. 44, no. 6, pp. 1255–1265, 2006.

[65] Kara K., Kim, D. and Morris, P. J., "Flow-separation Control Using Sweeping Jet Actuator," *AIAA journal*, vol. 56, no. 11, pp. 4604–4613, 2018, DOI: 10.2514/1.J056715.

[66] Tang G. and Agarwal R.K., "Numerical Simulation of Flow Control Over NASA Hump with Uniform Blowing Jet and Synthetic Jet," in *2018 Flow Control Conference*, pp. AIAA 2018–4017, DOI: 10.2514/6.2018–4017, 2018.

[67] Poisson-Quinton, P. and Lepage, L., "Survey of French Research on the Control of Boundary Layer and Circulation," *Lachmann, GV, Boundary layer and Flow Control. Its Principles and Application*, vol. 1, pp. 21–73, 1961, DOI: 10.1016/C2013-0-08248-5.

[68] Capizzano, F., Catalano, P., Marongiu, C. and Vitagliano, Pier Luigi, "U-RANS Modelling of Turbulent Flows Controlled by Synthetic Jets." AIAA Paper 2005-5015, 35th AIAA Fluid Dynamics Conference and Exhibit,Toronto, Ontario, Canada, 06 June 2005 - 09 June 2005, DOI: 10.2514/6.2005-5015.

[69] You, D., Wang, M. and Moin, P., "Large-eddy Simulation of Flow Over a Wall-mounted Hump with Separation Control," *AIAA journal*, vol. 44, no. 11, pp. 2571–2577, 2006, DOI: 10.2514/1.21989.

[70] Zhang, J., Xu, K., Yang, Y., Ren, Y., Patel, P., Zha, G., "Aircraft Control Surfaces Using Co-flow Jet Active Flow Control Airfoil." AIAA Paper 2018-3067, 2018 Applied Aerodynamics Conference, Atlanta, Georgia, June 25-29, 2018, DOI: 10.2514/6.2018-3067.